Mechanistic routes toward C3 products in copper-catalysed CO2 electroreduction

Supplementary Information

Mechanistic Routes Toward C_3 Products in Copper-Catalysed CO_2 Electroreduction

Sergio Pablo-García[a†], Florentine L. P. Veenstra[b†], Louisa Rui Lin Ting[c,d,†], Rodrigo García-Muelas[a], Antonio J. Martín[b], Federico Dattila[a], Boon Siang Yeo[c,d,*], Javier Pérez-Ramírez[b,*], Núria López[a,*]

a. Institute of Chemical Research of Catalonia, ICIQ, The Barcelona Institute of Science and Technology. Av. Països Catalans 16, 43007 Tarragona. Spain.

b. Institute for Chemical and Bioengineering, Department of Chemistry and Applied Biosciences, ETH Zürich, Vladimir-Prelog-Weg 1, 8093 Zürich, Switzerland.

c. Department of Chemistry, National University of Singapore, 3 Science Drive 3, Singapore 117543.

d. Solar Energy Research Institute of Singapore, National University of Singapore, 7 Engineering Drive 1, Singapore 117574.

† These authors contributed equally to this work.

**Corresponding author: chmyeos@nus.edu.sg; jpr@chem.ethz.ch; nlopez@iciq.es*

Experimental and Computational Details

Reagents

All reagents used are commercially available: acetaldehyde (33.7 µL, 50 mM, ≥ 99.5%, Sigma-Aldrich), formaldehyde (113 µL, 50 mM, 16% w/v in ultrapure water, methanol-free, Thermo Scientific Pierce), glyoxal (60.8 µL, 50 mM, 40 wt% in H_2O, Alfa Aesar), sodium oxalate (54 mg, 50 mM, 99.5%, Fluka BioChemika), ethanol (23.4 µL, 50 mM, 99.8%, Fischer Chemicals), ethylene glycol (22.4 µL, 50 mM, 98+%, Merck), sodium acetate (32.8 mg, 50 mM, 99+%, VWR Chemicals), methanol (16.2 µL, 50 mM, Fluka Analytical), carbon monoxide (99.997%, Air Liquide), propionaldehyde (44.6 µL, 50 mM, 97 %, Sigma-Aldrich) and allyl alcohol (41.2 µL, 50 mM, ≥ 99 %, Sigma-Aldrich).

Preparation of CuO-modified Cu foils

Cu foils (99.9%, 15×22×0.3 mm) were individually polished using a sequence of SiC paper (1200 µm grit) and alumina suspensions (0.3 µm and 0.05 µm), after which they were sonicated in water and then in ethanol and finally dried. The foils were then submerged in a one-compartment cell containing a freshly prepared electrodeposition bath under a two-electrode configuration. A constant current of 8 mA cm^{-2} was applied for 10 minutes to electrodeposit CuO. A Pt wire was used as the counter electrode. The electrodeposition bath was prepared by mixing L-tartaric acid (1.5 g, 99%, Sigma-Aldrich) and copper sulfate pentahydrate (2.5 g, ≥99%, Sigma-Aldrich) in 50 mL deionised water for 10 min, then adding sodium hydroxide (4.0 g, 99.99%, Sigma-Aldrich) to adjust the pH from 1.0 to 13.4.

Electrochemical measurements in 0.1 M potassium hydroxide

The electrocatalytic tests using various reagents were conducted using a three-electrode configuration in a custom-made gas-tight cell consisting of two compartments separated by a Nafion 211 membrane with gas-flow inlet and outlet ports. The cell was mounted with a gas diffusion layer (GDL) carbon paper acting as the counter electrode (Sigracet 39BC, SGL Carbon) and a CuO-modified Cu foil electrode (0.49 cm^2) as the working electrode. Before electrolysis, the working electrode was pre-reduced to OD-Cu for 5 min in pure N_2-purged electrolyte at −0.6 V *vs.* RHE. A leak-free Ag/AgCl electrode (3 M KCl, model LF-1, Innovative Instruments) served as the reference. The cathodic and anodic compartments contained 8 and 7.8 cm^3 of 0.1 M potassium hydroxide (pH 13), respectively. The catholyte was stirred at 400 rpm. A N_2 flow at a low rate of 2 cm^3 min^{-1} was bubbled separately into each compartment to maximize the concentration of the gaseous products, which resulted in a quasi-batch configuration during electrolysis. Both chambers were connected to syringes allowing for a slight expansion of the headspace to minimize pressure variations. The electrochemical measurements were conducted by an Autolab PGSTAT302N potentiostat at room temperature, with all potential values reported versus the RHE scale. The experiments were carried out with the R compensation function set at 85% of the uncompensated resistance R_u, determined by electrochemical impedance spectroscopy (EIS) measurements at high frequency (10 000 Hz). R_u was calculated every 10 min and used to continuously correct the applied overpotential during the entire 90 min electrolysis. Following this procedure, the applied potentials were within 10 mV of the target potential.

Electrochemical measurements in 0.1 M potassium phosphate buffer

The electrolysis experiments were performed in an H-type cell separated by an anion-exchange membrane (Selemion AMVN, AGC Asahi Glass). The cell was mounted with the CuO-modified Cu foil electrode (exposed geometric area of 0.785 cm^2) as the working electrode, Ag/AgCl reference electrode (saturated KCl, Pine), and graphite rod as the counter electrode. Before electrolysis, the working electrode was pre-reduced to OD-Cu for 5 min in pure N_2-purged electrolyte at −0.6 V *vs.* RHE. The cathodic and anodic compartments contained 12 and 8 cm^3 of 0.1 M potassium phosphate buffer (pH 7; 0.062 M K_2HPO_4 + 0.038 M KH_2PO_4), respectively. A N_2 flow of 5 cm^3 min^{-1} was separately bubbled into each compartment, with a continuous flow from the cathode chamber into an online GC (Agilent 7890A) for detection of gaseous products. The electrochemical measurement was performed using a Gamry Reference 600 potentiostat/galvanostat at room temperature and the current interrupt method was used to compensate for the *iR* drop throughout the 60 min electrolysis.

Electrochemical measurements in 0.1 M potassium bicarbonate

Electrolysis of CO_2 was performed in an H-type cell separated by an anion-exchange membrane (Selemion AMVN, AGC Asahi Glass). The cell was mounted with the CuO-modified Cu foil electrode (exposed geometric area of 0.785 cm^2) as the working electrode, Ag/AgCl as the reference electrode (saturated KCl, Pine) and graphite rod as the counter electrode. Before electrolysis, the working electrode was pre-reduced to OD-Cu for 5 min in N_2-purged electrolyte at −0.6 V *vs.* RHE. The cathodic and anodic compartments contained 12 and 8 cm^3 of 0.1 M $KHCO_3$ (99.99 %, Meryer), respectively. CO_2 was bubbled into each compartment at 20 cm^3 min^{-1}. The gases in the headspace of the cathode chamber were continuously flowed into an online GC (Agilent 7890A) for the detection of gaseous products. The electrochemical measurement was performed using a Gamry Reference 600 potentiostat/galvanostat at room temperature and the current interrupt method was used to compensate for the *iR* drop throughout the 60 min electrolysis.

Linear sweep voltammetry (LSV) was performed in N_2- and CO_2- purged 0.1 M $KHCO_3$ using the same cell setup as CO_2 electrolysis. Before the measurement, the CuO-modified Cu foil was pre-reduced to OD-Cu for 5 min in N_2-purged electrolyte at −0.6 V *vs.* RHE. The OD-Cu was then used as the working electrode for the LSV measurement. Ag/AgCl (saturated KCl, Pine) was used as the reference electrode and a graphite rod was used as the counter electrode. The electrolyte was purged with N_2 or CO_2 for at least 30 min before being used for experiments. During the measurement, the cell was continuously purged with N_2 or CO_2 at a rate of 20 cm^3 min^{-1}. The scan rate used was 5 mV s^{-1}. The electrochemical measurement was performed using a Gamry Reference 600 potentiostat/galvanostat at room temperature, with the current interrupt method used to compensate for the *iR* drop.

Catalyst characterisation

X-ray diffraction (XRD) was performed with a Siemens 5005 (Cu$K\alpha$ radiation with graphite monochromator), in locked θ-2θ scan mode from 20 to 100° 2θ with 0.1° resolution step and 1 second acquisition time per step.

Product analysis

Liquid products formed during electrolysis in 0.1 M KOH were quantified by ^{1}H-NMR. Following the reaction, catholyte and anolyte samples (0.7 cm^3) were each mixed with D_2O (0.05 cm^3) containing phenol (50 mM) and dimethyl sulfoxide (50 mM) as internal standards. 1*D* ^{1}H-NMR spectra of the sample with water suppression were recorded on a Bruker Avance III HD 500 MHz mounted with a 5 mm BBO Prodigy (at room temperature). Pulse experiments were pre-saturated on the water resonance with a π/2 pulse of 12 µs (at a power of 15.9 W, accounting for -12.1 dB) and a recycle delay of 5 s (with pre-set power of 9.2×10^{-5} W accounting for 40.38 dB) was implemented while co-adding 256 scans per experiment. These settings resulted in a high signal-to-noise ratio and an analysis time of *ca.* 35 minutes per sample. The detection limit is 0.5 µM.

Propylene production during electrolysis in 0.1 M KOH was quantified by headspace gas chromatography-mass spectrometry (GC-MS). All GC-MS measurements were conducted using Agilent 7890B (G3440B) GC connected to Agilent 5977A (G7039A) MS. The 20 mL headspace vials (Agilent 5188-2753 Hdsp cap 18 mm magnetic PTFE/Sil Agilent 5188-2759) were placed in an autosampler (PAL RSI 120 G7368-64100). All separations were carried out using helium carrier gas over an Agilent 121-5522LTM DB column. The detection limit is around 0.1 ppm.

Gaseous products formed during electrolysis in 0.1 M potassium phosphate buffer (pH 7; 0.062 M K_2HPO_4 + 0.038 M KH_2PO_4) and 0.1 M $KHCO_3$, were quantified using on-line GC with flame ionisation detector (FID) and thermal conductivity detector (TCD) sampling every 19.6 min. The detection limit is 0.5 ppm, which is equivalent to a production rate of 0.5 µmol cm^{-2} h^{-1}. Liquid products were quantified using headspace gas chromatography (HSGC) and high-performance liquid chromatography (HPLC). Alcohols and carbonyl compounds were analysed by HSGC (Agilent, 7890B and 7697A). The detection was performed by FID, with a detection limit of 0.2 µM, equivalent to a production rate of 0.3 mol cm^{-2} h^{-1}. HPLC analysis of formate and acetate was conducted using Agilent 1260 Infinity with a variable wavelength detector (VWD), using 0.5 mM sulfuric acid (96% Suprapur, Merck) as the mobile phase. The resulting detection limit is 2 µM, corresponding to a production rate of 3 mol cm^{-2} h^{-1}.

Density Functional Theory

Periodic DFT calculations were performed with the Vienna Ab-initio Simulation Package (VASP)[1] and Perdew–Burke-Ernzerhof (PBE)[2] density functional including van der Waals D2 corrections[3]. To avoid the over-binding tendency of the D2 method, we employed our reparametrised C_6 coefficients for the metals[4]. Core electrons were represented by PAW[5] while valence electrons were expanded in plane waves with a kinetic cut-off energy of 450 eV. The Cu surface was modelled as a four-layer Cu(100) slab, the most stable surface at working potentials[6,7]. The Brillouin zone was sampled by a Γ-centered k-points mesh from the Monkhorst-Pack method with a reciprocal grid size smaller than 0.03 $Å^{-1}$. Transition states were identified from the climbing image version of the Nudged Elastic Band (CI-NEB) method[8]. All structures were converged by forces, using as thresholds 0.02 and 0.05 eV $Å^{-1}$ for adsorbates and transition states, respectively. Computed structures are available through the

ioChem-BD database[9,10]The solvent was introduced through our in-house developed implicit model, VASP-MGCM[11,12]. The Computational Hydrogen Electrode (CHE)[13,14] was used as the electrochemical model. Accuracy tests on density functionals (comparing PBE-D2 barriers with BEEF-vdW), LSR, and charge analysis are described in **Note S6** and **Figures S6-S9**.

Automatic generation of intermediates

Due to the high number of species involved, around 500, the intermediates of the reaction network were automatically generated. First, we started with fully hydrogenated C_1–C_4 molecules: methane, methanol, formic acid, acetic acid, ethane, ethanol, ethylene glycol, 1-propanol, 2-propanol, 1,2-propanediol, and 1,3-propanediol. To generate the different intermediates throughout the network, we took the molecules in the previous list as energy references and converted them to graphs[15] where each node represents an atom, labelled with its element, and the edges represent the bonds between atoms, each for one structure (s-graph). Then, the following steps are performed recursively:

1) a hydrogen node from the graph is selected;
2) the hydrogen atom is removed by generating a subgraph without the selected node;
3) an isomorphism test is performed to compare the subgraph with the rest of the generated subgraphs thus avoiding chemically equivalent geometries;
4) if no equivalent subgraphs are found, the subgraph is stored along with its connection to its mother graph;
5) repeat the process on the newly generated subgraphs until no hydrogen nodes are found in the subgraph.

With the connectivity information, all structures are then adjusted to their most likely adsorption conformations, **Note S8**, and their energies are explicitly evaluated with DFT. Related methodologies to explore complex routes have been put forward for the CO_2 hydrogenation to starches[16] in thermo- and biocatalysis.

Formation energies of intermediates and transition states

The energies as obtained by VASP ($E_{C_xH_yO_z*,\mathrm{VASP}}$) were initially written as a function of the clean surface, CO_2, water, and hydrogen as energy references, **Eq. S1-S2**. Following the CHE formalism, the DFT energy of H^+ (E_{H^+}) at the RHE scale is approximated as ½H_2 (as obtained from VASP, $E_{H_2,\mathrm{VASP}}$). The result inside the curly brackets of **Eq. S2** is herein called DFT energy ($E_{C_xH_yO_z*,\mathrm{DFT}}$). Implicit solvation[11,12] (E_{solv}) and polarisation[17] corrections ($\Delta Q_B \cdot U$) were then applied to get the potential energies used throughout the Manuscript ($E_{C_xH_yO_z*}$, or E in shorthand notation, **Eq. S2**). The energy related to electron transfers equals the number of electrons transferred times the electric potential U. Some molecules drag electronic density from the surface; for instance, adsorbed OH has around 8 electrons, obtained from their Bader charges (benchmarked against Mulliken or dipole derived provide similar estimates), instead of the nominal charge of the neutral fragment 7 than would be employed in the standard CHE approach[18,19]. Thus, the external potential contribution, written as $-(2x+y-z)e^- U$, requires an additional polarisation term $\Delta Q_B \cdot U$ that has been then added as a correction to the DFT energy,

Eq. S2. To assess the validity of the Bader polarisation term, charge estimates were performed with two alternative methodologies, taking derived from the dipole correction and Mulliken population analyses respectively, **Note S6** and **Figures S8-S9**. The tests demonstrate that the choice of Bader charges is reasonable besides easier to implement.

$$x\cdot CO_2 + \left(z-2x\right)H_2O + \left(2x+y-z\right)H^+ + \left(2x+y-z\right)e^- + * \rightarrow C_xH_yO_z* \quad \text{(S1)}$$

$$E_{C_xH_yO_z*,\mathrm{DFT}} = E_{C_xH_yO_z*,\mathrm{VASP}} - E_{*,\mathrm{VASP}} - xE_{CO_2,\mathrm{VASP}} + (2x-z)E_{H_2O,\mathrm{VASP}} + (-2x-y+z)E_{H^+} + (-2x-y+z)e^-U \quad \text{(S2)}$$

$$E_{H^+} = \tfrac{1}{2}E_{H_2,\mathrm{VASP}} \quad \text{(S3)}$$

$$E \equiv E_{C_xH_yO_z*} = E_{C_xH_yO_z*,\mathrm{DFT}} + \Delta Q_B \cdot U + E_{\mathrm{solv}} \quad \text{(S4)}$$

Reaction energies and barriers were then obtained from **Eq. 3**-**4**, where E_{IS}, E_{FS}, and E_{TS} represent the energies of initial, final, and transition states respectively. As uncertainty in such quantities may affect selectivity trends[20–23], all relevant transition states were explicitly calculated *via* DFT. These include all 586 C_1–C_2 couplings and 8 C–H/O–H hydrogenations and 10 C–O(H) bond breakings from CH_2CHCHO to propanol and propylene. The remaining energies for C–H and O–H hydrogenations were approximated from LSR available for Cu[15], **Eq. 5** and **Table S15**. These equations also hold in solvated environments[12]. We found that, for C–H and O–H hydrogenation reactions, LSR describe with sufficient accuracy our DFT results, **Figure S7**. Differences in Bader charges upon reaction, shown in **Table S18**, were calculated from **Eq. 6**, and typically ranges between –0.3 to +0.7 e^- (**Table S18**). When constructing the energy profiles (**Figure 4-5**, **S4-S5**, **S10-S15**), we considered that all hydrogenations as Tafel-like elementary steps, except from O or OH stripping, which involves a Heyrovsky-like step, **Note S5**.

$$\Delta E = E_{FS} - E_{IS} \quad \text{(S5)}$$

$$E_a = \max\left(E_{IS}, E_{FS}, E_{TS}\right) - E_{IS} \quad \text{(S6)}$$

$$E_{TS,LSR} = \left(1-\alpha\right)E_{IS} + \alpha E_{FS} + \beta \quad \text{(S7)}$$

$$\Delta\Delta Q_B = \Delta Q_{B,FS} - \Delta Q_{B,IS} \quad \text{(S8)}$$

Graph representation of the reaction network

The intermediate generation procedure keeps track of all the dehydrogenation reactions. Additionally, we also considered C–C, C–O, and C–OH bond breakings and formations. Then, each intermediate subgraph:

(1) is split into two different fragments (subgraphs) depending on the selected bond breaking,

(2) each generated fragment is compared with the subgraphs with matching elements from other families,

(3) if an equivalent structure is found, then the connection between the subgraphs is stored.

The information of the intermediates and their connections are then stored in a directed network graph, n-graph[24]. In this n-graph, the intermediates correspond to the nodes and the edges are the reactions.

Supplementary Notes

Note S1: On the analysis of the reaction network

We detail below the total number of intermediates and transition states that were computed explicitly by DFT. Originally, 463 intermediates were considered:

- 17 of them were C_1[19,25],
- 55 C_2[15],
- 387 C_3, and
- 4 that did not contain any C atom (H_2O, OH, O, H).

Among the C_1, 5, 8, and 4 came from the dehydrogenation of methane (CH_4), methanol (CH_3OH), and formic acid (HCOOH) respectively.

Among the C_2, 10, 24, and 21 came from the networks of ethane, ethanol, and ethylene glycol respectively.

Among the C_3, 30 (28), 72 (70), 40 (28), 98 (83), 63 (61), and 84 (77) came from the dehydrogenation of propane, 1-propanol, 2-propanol, 1,2-propylene glycol, 1,3-propylene glycol, and glycerol respectively.

The numbers in parenthesis indicate the intermediates that converged to the desired structure. Thus, 40 C_3 intermediates did not converge, and the elementary steps associated were removed from the reaction network.

The 463 well-converged C_1–C_3 intermediates are interlinked by a network containing 2266 steps, out of which 604 (27%) were fully characterised *via* DFT. A total of 691 were C–C couplings. Among them, 55 and 636 were C_1–C_1 and C_1–C_2 couplings, respectively, that yield C_2 and C_3 intermediates (C_2: **Figure S5**, C_3: **Tables S16-S18**). Originally, we had considered that 10 C_1 and 70 C_2 moieties could combine to produce a C_3 species. Nevertheless, as only 347 of 387 C_3 intermediates converged, only 636 (instead of 700) couplings were deemed possible. From them, 586 converged to the desired transition states. The remaining 114 are left void in **Tables S16-S18**. Further details about selected C_1–C_2 couplings are shown in **Table S19**.

Besides, there were 286 C–O and 301 C–OH bond-breaking reactions. 10 of them (5 C–O and 5 C–OH) were calculated using DFT-NEB (**Table S20**). Regarding hydrogenations, there were 683 C–H and 305 O–H bond formations, 8 of them (4 C–H and 4 O–H) computed *via* DFT-NEB (**Table S21**). The remaining hydrogenations were approximated *via* LSR, which have low error bars for hydrogenation processes as extensively shown in the literature and also since the TS energy is mainly assigned to the activation of H to on-top positions[15,25,26], **Figure S7**. Heyrovsky-like variations were also considered for the 301 C–OH breakings and 305 O–H hydrogenations, **Note S5**.

Note S2: Computing the transition states for the C_1–C_2 bond formation

For each C_1–C_2 bond formation, we took the ground state of the C_3 product as the final state. Then the initial states were approximated by separating the two moieties until the carbon atoms were at a distance of 3.5 Å. To avoid the molecules getting too close or too far to the surface, this elongation was made parallel to the *xy* plane, and both moieties were then shifted 0.2 Å down along z. These initial states were then relaxed during 30 steps to reduce tensions, but explicitly avoiding a full relaxation. Four images were generated for all reactions. Then, the

NEB algorithm was applied as implemented in VASP-VTST and analysed with the script of Prof. Henkelman's group[8,27,28].
When the predicted transition state was at a distance ±10% of a given image, we switched to CI-NEB. Else, we generated a new NEB by zooming the interval around the predicted maximum. Yet, for 117 reactions, the minimum-energy path was monotonously going down without a clear maximum. They are marked as * in **Table S15**.

Note S3: Efficiency of automation in DFT

The explicit computation of transition states by density functional theory (DFT) is highly costly in terms of human hours, as close to 30% of all runs fail to converge when using automation[29]. This translates into 260-700 out of 2266 transition states requiring human intervention if all of them were to be calculated with DFT, even when using automated workflows for NEB calculations.

Note S4: Extension of the graph network for C_{3+}

Strategies proposed in this work can be extended for C_{3+} networks. However, as the number of reactions and intermediates exponentially increases with an increasing number of carbons, a screening process may be needed to handle the complexity of the network due to the massive computational resources needed to compute both intermediates and transition states with DFT. For example, for the C_4 network, the number of intermediates increases from 463 to more than 700 and the number of transition states almost doubles from 2266 to more than 3900. In this work, we demonstrated that only a small domain of the reactivity graph is responsible for the selectivity for desired products, and thus, only this domain needs to be strongly evaluated *via* DFT. Hence, a thermodynamic exploration of the reaction intermediates, discarding the reactions highly endothermic (or in a second step with high energy barriers) and only evaluating key domains of the reaction graph may be the appropriate approach to explore C_{3+} networks.

Note S5: Heyrovsky and Tafel-like steps in energy profiles

When constructing the energy profiles, we considered that all hydrogenations occur from adsorbed H*, in Tafel-like elementary steps, **Eq. S9**. However, to strip O or OH groups, one hydrogenation was considered to go through a Heyrovsky-like step, **Eq. S10-S11**, respectively. Specifically, we used the energies derived from **Eq. S12** for all figures dealing with C_3 compounds (**Figure 2, 4**, **S10-S11** and **Tables S16-S18**), and **Eq. S13** for **Figure S4**. H^+ is considered a reference value, and its DFT energy is set to 0 for the calculation of LSR.

$$C_xH_yO_z{*}+H{*} \rightarrow C_xH_{y+1}O_z{*} + {*} \quad \text{(S9)}$$

$$C_xH_yO_z{*}+H^+{+}e^-{+}H{*} \rightarrow C_xH_yO_{z-1}{*} + H_2O + {*} \quad \text{(S10)}$$

$$C_xH_yOH{*}+H^+ + e^- \rightarrow C_xH_y{*} + H_2O \quad \text{(S11)}$$

$$CH_2CHCO{*}+5H{*}+H^+{+}e^- \rightarrow C_3H_xO_y{*}+(1-y)H_2O_{(aq)}+y(H^+{+}e^-)+(7+y-x)H{*}+(x-y-2){*} \quad \text{(S12)}$$

$$OCCO{*}+8H{*}+2(H^+{+}e^-) \rightarrow C_2H_xO_y{*}+(2-y)H_2O_{(aq)}+y(H^+{+}e^-)+(6+y-x)H{*}+(x-y+2){*} \quad \text{(S13)}$$

Note S6: Charge Benchmarking

Charge displacement obtained from dipole moments

As an alternative to Bader analysis, a proxy of the charge taken by an adsorbate upon adsorption can be deduced by the arising net electric dipole of the adsorbate-metal system, $\vec{\mu}_{\text{tot}}$ in **Eq. S14**. We first decomposed such dipole into three components. The first one is intrinsic of the asymmetric slab model used in DFT, $\vec{\mu}_{*}$. The second one is intrinsic of the adsorbate A by excluding all perturbations caused by the surface, $\vec{\mu}_{A}$. Upon adsorption, the charge density taken by A from the surface ($Q_{A*} - Q_{A}$) creates a third contribution $\vec{\mu}_{\text{ads}}$, **Eq. S15**. Thus, the net charge transfer ΔQ_{d} can be approximated from **Eq. S16**. Here z_{A} was obtained from the average height of all atoms in the adsorbate (C, H, O). while z_{*} is the position of the outermost Cu layer. The dipole moments were obtained from the Neugebauer and Scheffler corrections as given by VASP, applied along z[30]. The net charge transfer obtained by this method is comparatively smaller than that obtained from Bader analysis by a factor of 0.24, **Figure S8**. The ¼ factor was found by Lang and Kohn when describing the interaction of a punctual charge and its induced surface charge in the metal[31].

$$\vec{\mu}_{\text{tot}} = \vec{\mu}_{*} + \vec{\mu}_{A} + \vec{\mu}_{\text{ads}} \tag{S14}$$

$$\vec{\mu}_{\text{ads}} = \left(Q_{A*} - Q_{A}\right)\left(z_{A} - z_{*}\right)\hat{z} \tag{S15}$$

$$\Delta Q_{\text{d}} \equiv Q_{A*} - Q_{A} = \frac{\left\|\vec{\mu}_{\text{tot}} - \vec{\mu}_{*} + \vec{\mu}_{A}\right\|}{z_{A} - z_{*}} \tag{S16}$$

Relation between Bader and Mulliken charges

Another proxy of the charge transferred upon adsorption is the increments in Mulliken charges, Q_{M}. Such quantity is calculated from the Mulliken charge around the atoms of the adsorbate, A, in the adsorbed structure ($Q_{\text{M,A@A*}}$) versus the same structure put in the gas phase ($Q_{\text{M,A,gas}}$), **Eq. S17**. These values are prone to arbitrariness in the definition of the Wigner–Seitz radii (r_{WS}). Here we took the default r_{WS} values included in the PAW files. **Figure S9** shows that increments in Mulliken charges underestimate Bader values, which is to be expected as the integration volume is significantly lower.

$$\Delta Q_{\text{M}} \equiv Q_{\text{M,A@A*}} - Q_{\text{A,gas}} \tag{S17}$$

Note S7: Reaction conditions

The conditions of –0.95 V *vs*. RHE and 0.1 M $KHCO_3$ were chosen to maximize the Faradaic efficiency of multi-carbon products using oxide-derived copper from CO_2 [32]. As for the co-reduction experiments, a mild potential of −0.40 V *vs*. RHE was applied in a strongly alkaline pH (0.1 M KOH). Such conditions have been linked to increased C–C coupling rates [33].

As for the case of aldehydes, they undergo side reactions at alkaline pH, as demonstrated elsewhere [34]. For example, acetaldehyde is not stable in strongly alkaline pH, as it deprotonates to the ethenyloxy anion (CH_2CHO–) which in turn is reactive to competing pathways not leading to C_3 products. Ethenyloxy undergoes aldol condensation with the remaining acetaldehyde to produce crotonaldehyde and 1-butanol. The aldehydes can also be hydrated to form diols, which are electrochemically inactive. Thus, for experiments where aldehydes

were used, a neutral pH buffer (PPB) was used as the supporting electrolyte. Additionally, –1.00 V *vs*. RHE has also been identified as the optimal potential for propylene production from the co-reduction of formaldehyde and acetaldehyde, see **Table S3**.

Note S8: Conformational Search

Even simple C_2-C_3 adsorbates could have 10^1-10^2 conformations. Thus, we followed a simplified conformational analysis based on the heuristic rules devised in ref. [25,35]. These rules can be summarised as follows:

(i) The unsaturated bonds were placed close to the surface;
(ii) Oxygen atoms were also placed close to the surface;
(iii) Intermediates containing at least two oxygen atoms that can form intramolecular hydrogen bonds were put maximised their number of intramolecular hydrogen bonds;
(iv) Carbon tails face the surface;
(v) If the intermediate has cis-trans isomers, both were calculated, but only the most stable one was retained for subsequent analysis;
(vi) If the intermediate did not converge to a reasonable structure (for instance, very unsaturated C_3 structures generated cyclopropane analogues), the molecule was readjusted manually, trying up to 6 conformations that preserve the rules (i-iv).

Note S9: Linear Scaling Relationships for C_1–C_2 couplings

All transition state energies were originally estimated using Linear Scaling Relationships (LSR) from **Table S15**. As derived from these values, **Eq. S18** approximates all activation energies as 0.64 eV for all C–C couplings. Due to this lack of sensitivity, all C_1–C_2 coupling reactions were calculated explicitly using the NEB method (**Note S1**).

$$E_{TS} = E_{C1} + E_{C2} + 0.64 \text{ eV} \quad \text{(S18)}$$

Supplementary Figures

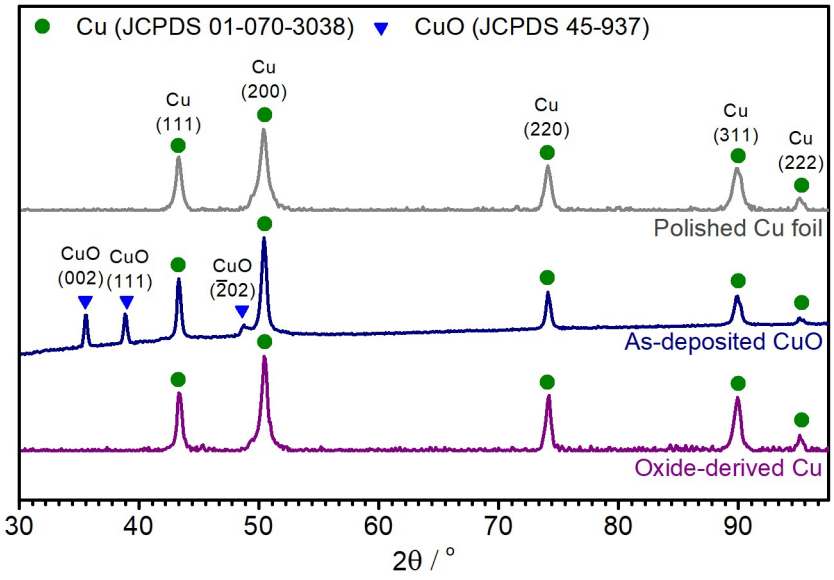

Figure S1. XRD patterns of as-deposited CuO (navy line) and OD-Cu (purple line). The peaks were assigned using standard XRD patterns JCPDS 01-070-3038 (Cu, green circle) and JCPDS 45-937 (CuO, blue triangle). The metallic Cu peaks in the as-deposited CuO come from the metallic Cu foil (grey line) used as the substrate for electrodeposition. The absence of CuO peaks in OD-Cu confirms that the oxide phase has been reduced to metallic Cu during pre-reduction.

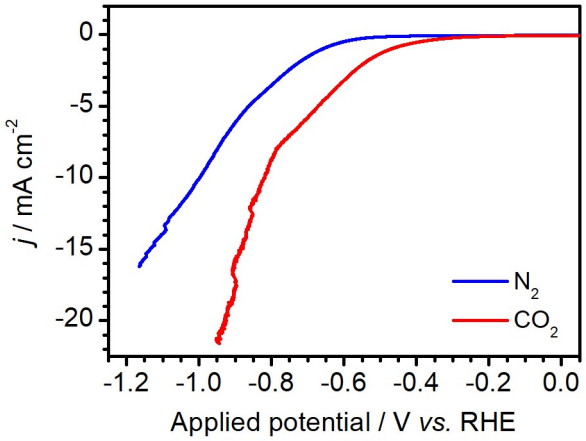

Figure S2. Linear sweep voltammograms of OD-Cu in N_2 (blue) and CO_2 (red) purged 0.1 M $KHCO_3$. The scan rate used was 5 mV s^{-1}. Note that in the CO_2 purged electrolyte, the electroreduction current is larger than when N_2 was the purging gas. This shows the activity of OD-Cu in catalysing eCO_2R.

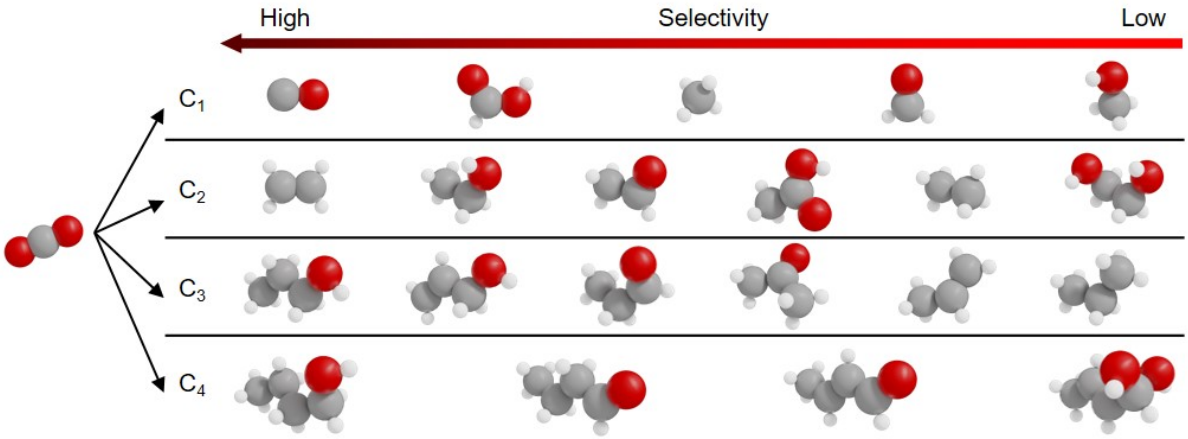

Figure S3. Overview of main C_1 - C_4 products in eCO_2R using copper-based catalysts[33,34,36]. Propylene (C_3H_6) is observed at very low selectivity compared to 1-propanol (C_3H_7OH). This is not a rigid classification, since observed selectivity trends are dependent on electrolysis conditions, especially for the case of C_1 products.

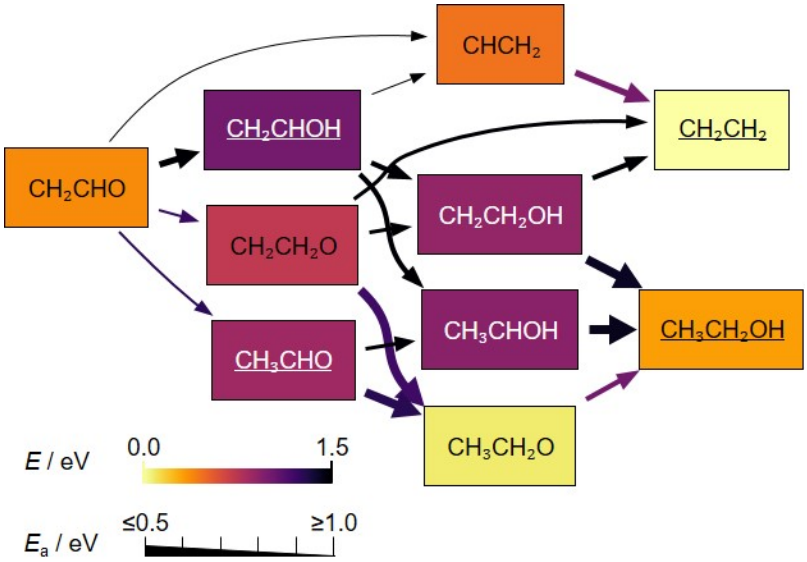

Figure S4. Energy profile for CH_2CHO hydrogenation to ethanol and ethylene at –0.4 V *vs.* RHE. The boxes represent intermediates with the colour-code indicating their relative potential energies (**Eq. S3**). The thickness of the arrows is linked to their activation energies (E_a), estimated from LSR. Underlined intermediates can also desorb into the solution.

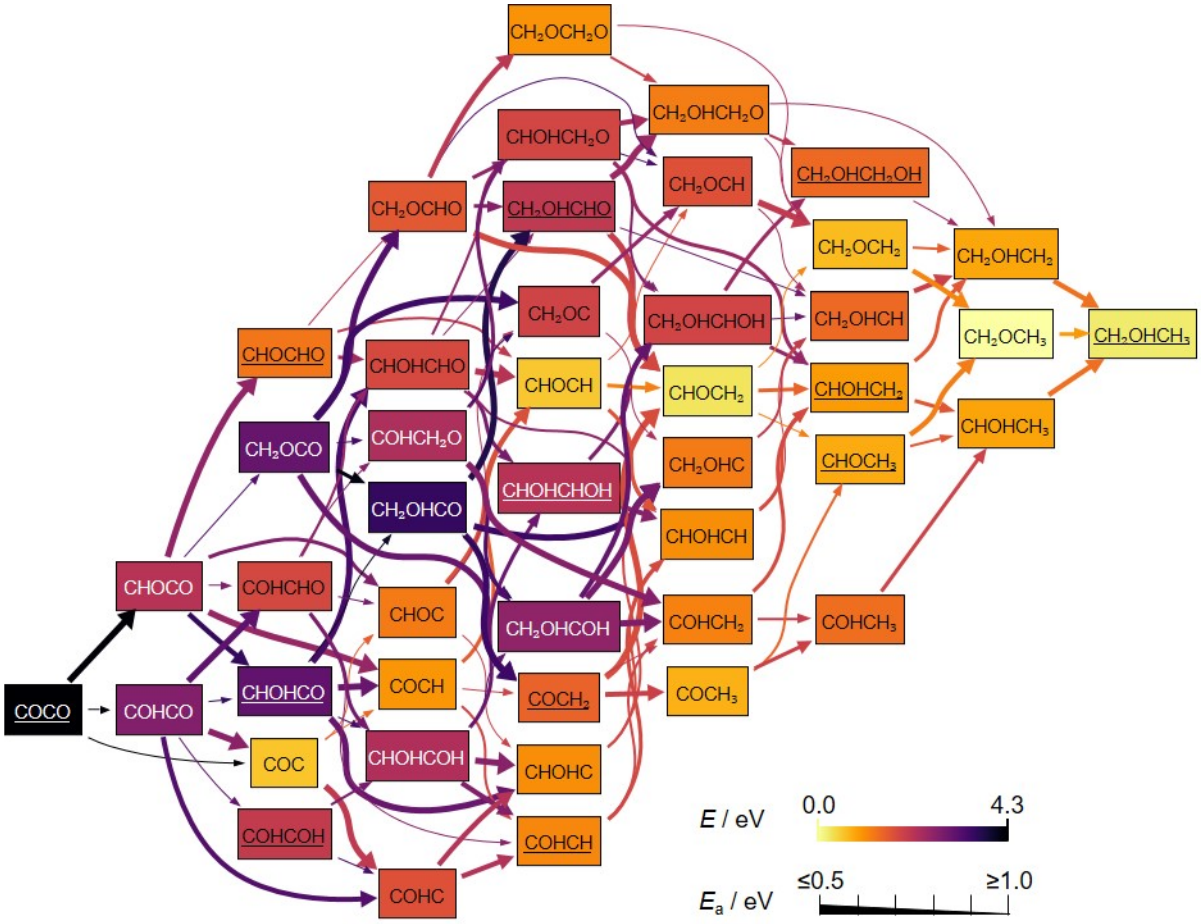

Figure S5. Energy network for OCCO hydrogenations to main oxygenated C_2-products at –0.4 V *vs.* RHE. The boxes represent intermediates with the colour-code indicating their relative potential energies (**Eq. S3**). The thickness of the arrows is linked to their activation energies (E_a), estimated from LSR. Underlined intermediates can also desorb into the solution.

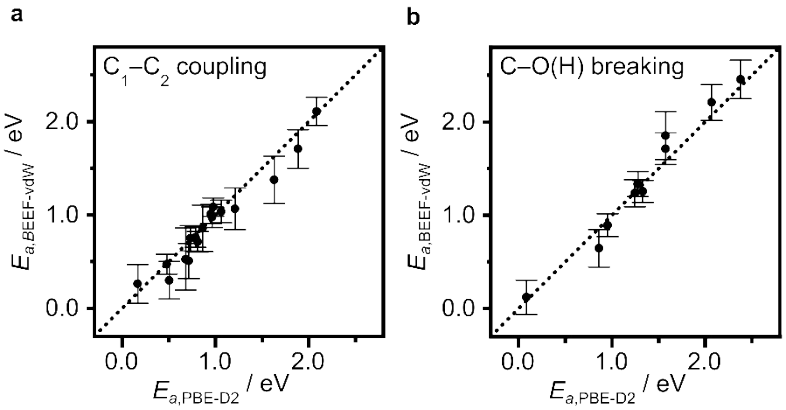

Figure S6. Parity plot of activation energies calculated with PBE-D2 *vs*. the corresponding values of BEEF-vdW including error bars for **a** C–C coupling and **b** C–O(H) breakings. PBE-D2 values taken from $E_{a,DFT}$ in **Tables S19-S20**.

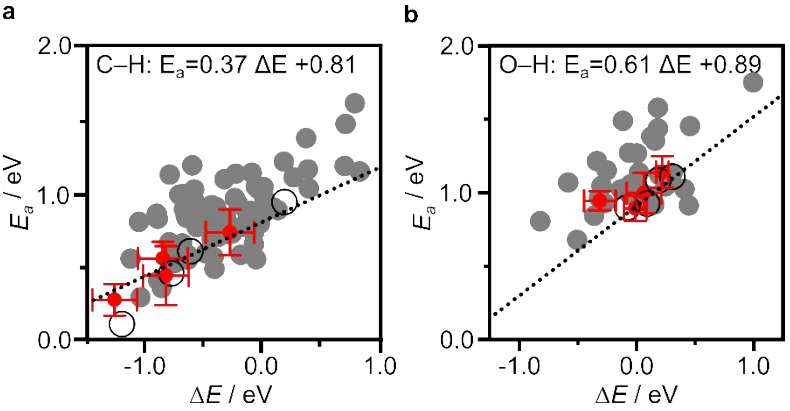

Figure S7. Linear-scaling relationships[15] for C–H and O–H hydrogenations (grey) compared to selected PBE-D2 (black) and BEEF-vdW values (red). The path selected was $CH_2CHCO \rightarrow CH_2CHCHO \rightarrow CH_3CHCHO \rightarrow CH_3CH_2CHO \rightarrow CH_3CH_2CH_2O$ and the protonation of the later four. BEEF-vdW error bars in ΔE and E_a are included.

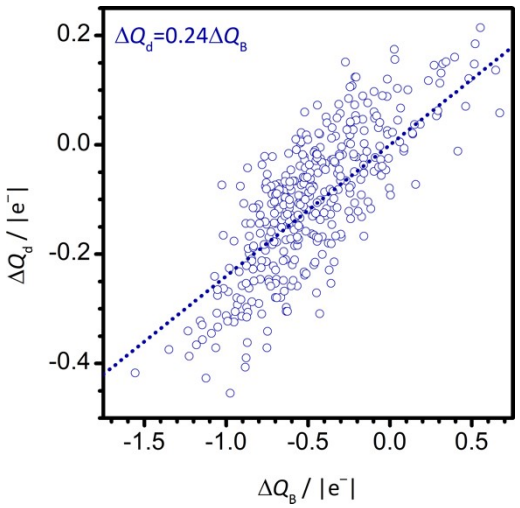

Figure S8. Parity plot of Bader charges *vs*. charges deduced from increments upon adsorption in the dipole moment along *z*. Best linear fit without independent term added as a guide to the eye.

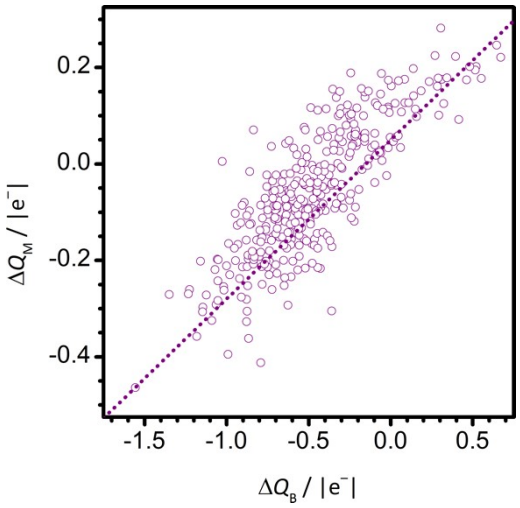

Figure S9 Parity plot of Bader charges *vs*. Mulliken charges upon adsorption. Line added as a guide to the eye.

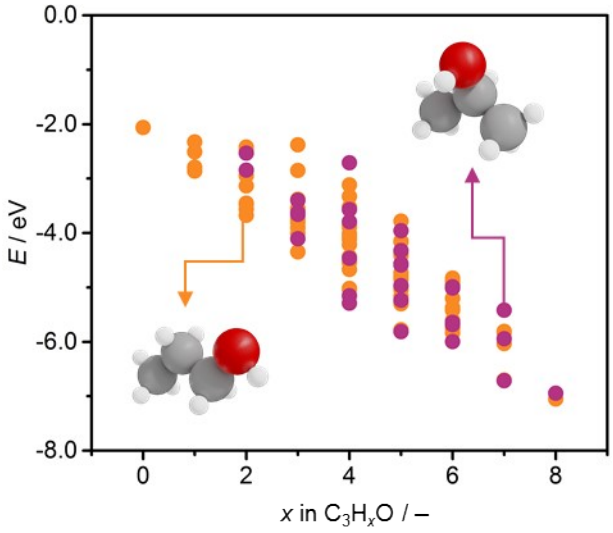

Figure S10. Energy of intermediates that share 1-propanol (orange) and 2-propanol (purple) backbones as a function of the number of hydrogens of the intermediate. For a given hydrogenation degree, the most stable intermediates of both backbones are comparable in energy.

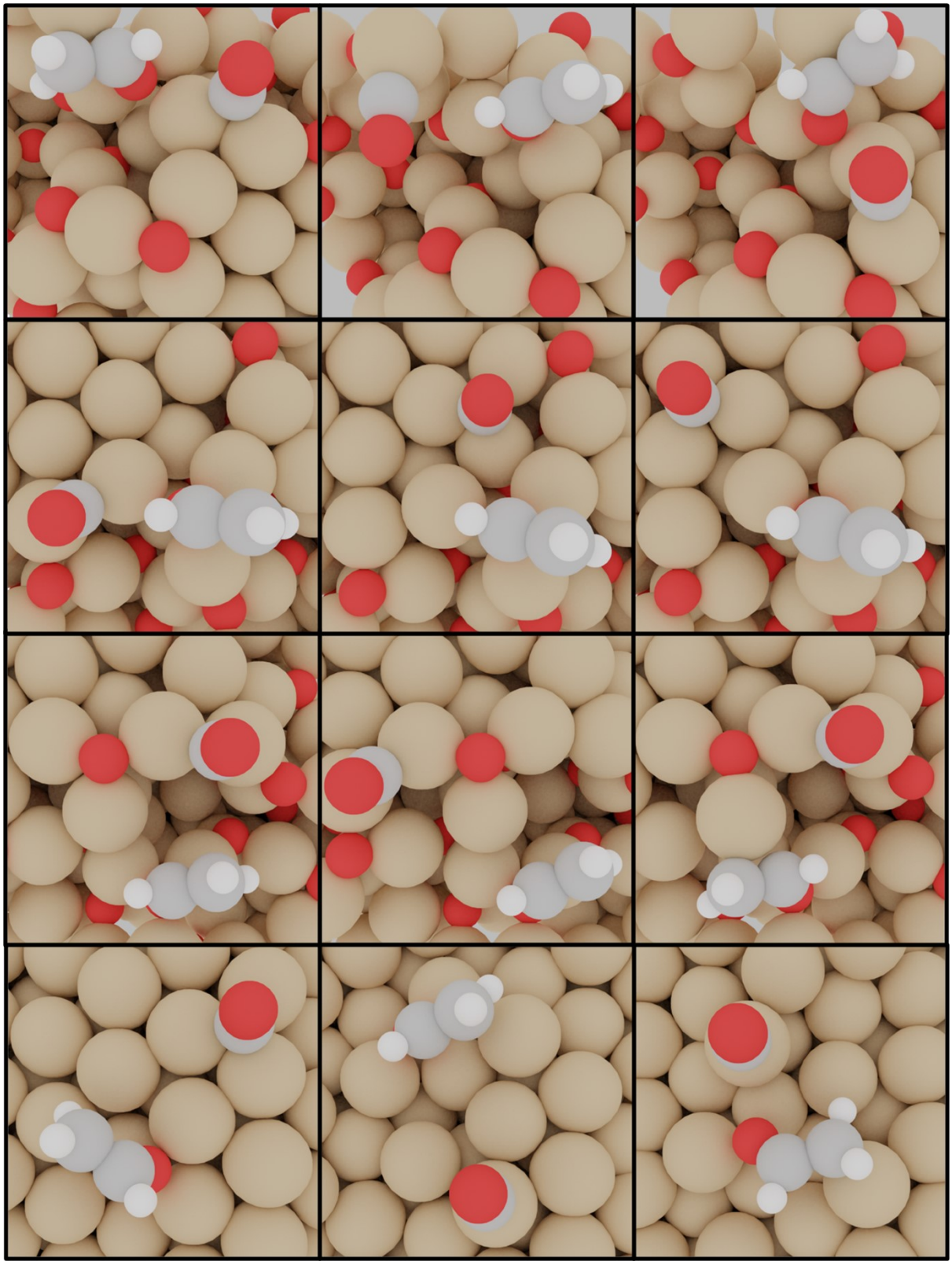

Figure S11 CH_2CHO-CO coupling configurations on 12 structural motifs formed on oxide-derived Cu models.[37,38] The most suitable active site for promoting this step is reported in **Figure 3**.

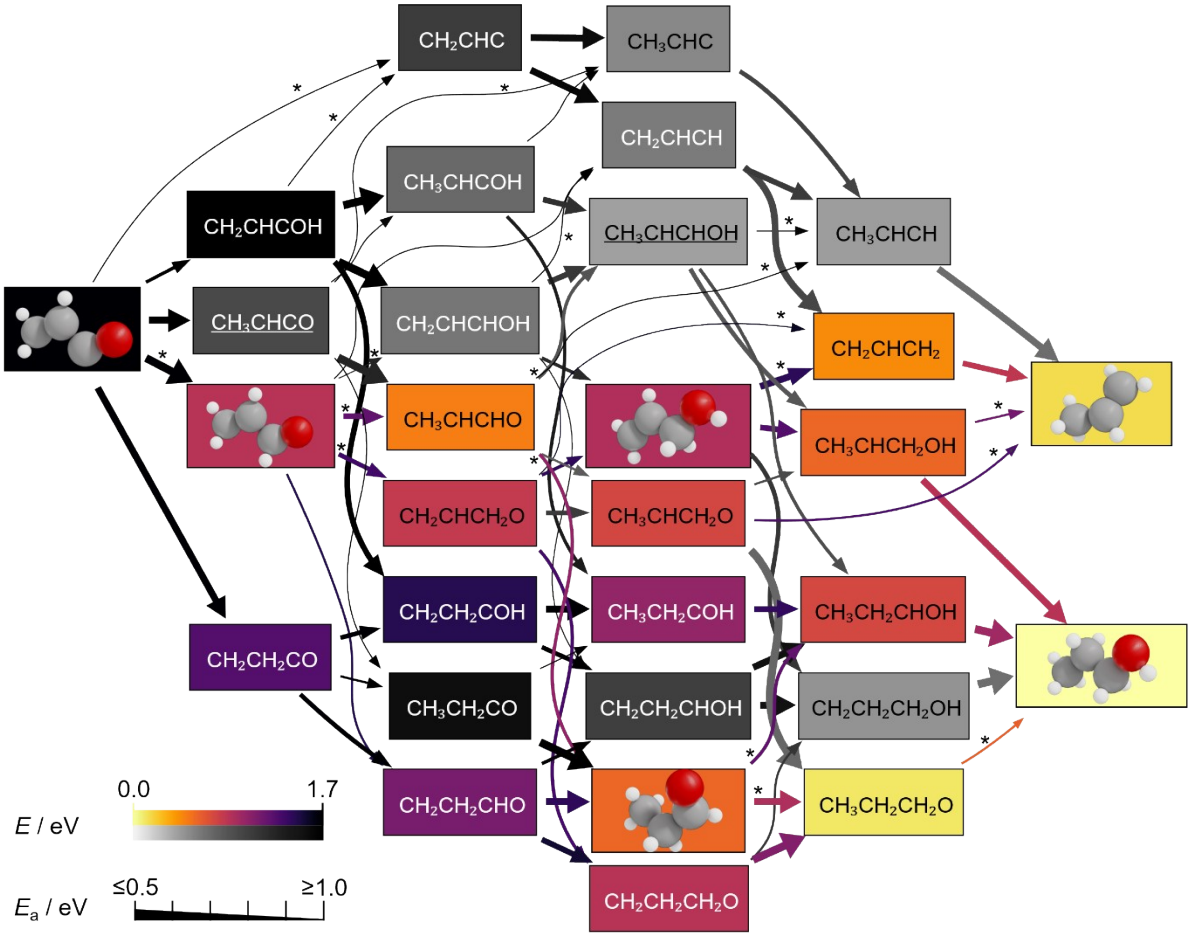

Figure S12. Energy profiles for hydrogenation of CH_2CHCO and CH_2CHCHO to propylene (C_3H_6) and 1-propanol (C_3H_7OH) at 0.0 V *vs*. RHE. The boxes represent intermediates with the colour-code indicating their relative potential energies (**Eq. S3**). Grayscale was used for the paths that are overall less favoured. The thickness of the arrows is linked to their activation energies (E_a), estimated from LSR (those marked with * correspond to explicitly calculated by DFT). Underlined intermediates can also desorb to the solution, among which, allyl alcohol (C_3H_5OH) and propionaldehyde (C_3H_6O) were used as reactants in experiments to probe theoretical predictions (**Figure 5**).

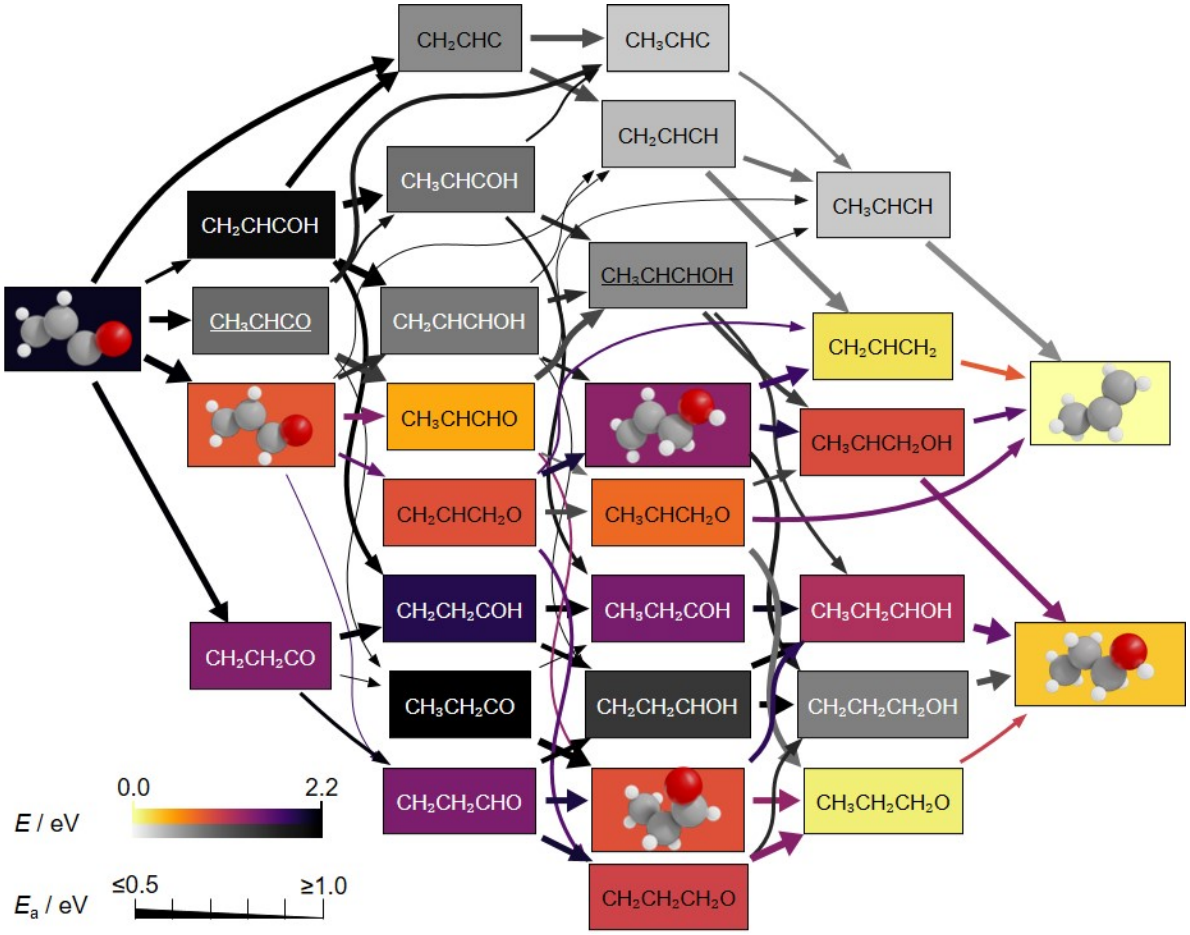

Figure S13. Energy profiles for hydrogenation of CH_2CHCO and CH_2CHCHO to propylene (C_3H_6) and 1-propanol (C_3H_7OH) at –0.4 V *vs*. RHE. The boxes represent intermediates with the colour-code indicating their relative potential energies (**Eq. S3**). Grayscale was used for the paths that are overall less favoured. The thickness of the arrows is linked to their activation energies (E_a). Underlined intermediates can also desorb to the solution, among which, allyl alcohol (C_3H_5OH) and propionaldehyde (C_3H_6O) were used as reactants in experiments to probe theoretical predictions (**Figure 5**).

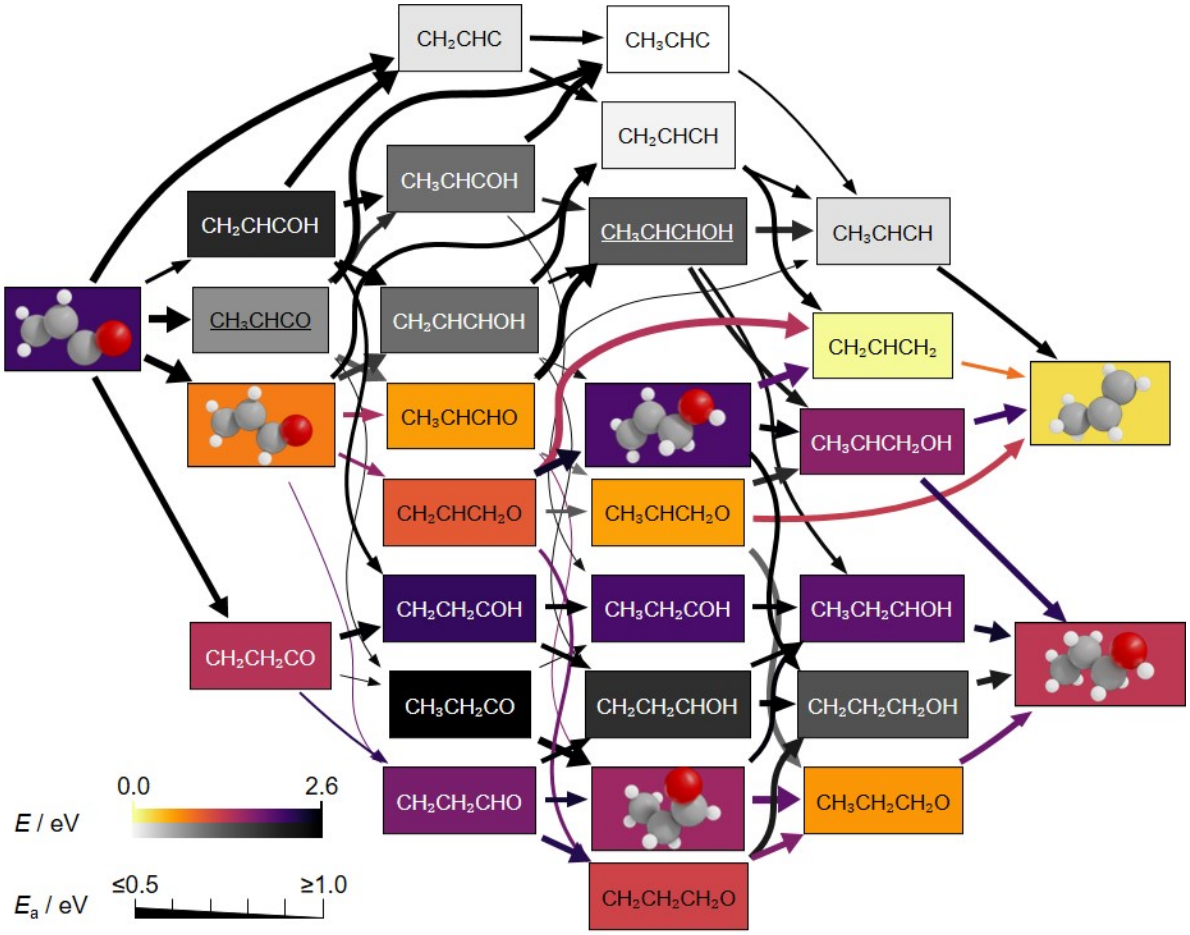

Figure S14. Energy profiles for hydrogenation of CH_2CHCO and CH_2CHCHO to propylene (C_3H_6) and 1-propanol (C_3H_7OH) at –1.0 V *vs*. RHE. The boxes represent intermediates with the colour-code indicating their relative potential energies (**Eq. S3**). Grayscale was used for the paths that are overall less favoured. The thickness of the arrows is linked to their activation energies (E_a). Underlined intermediates among which, allyl alcohol (C_3H_5OH) and propionaldehyde (C_3H_6O) were used as reactants in experiments to probe theoretical predictions (**Figure 5**).

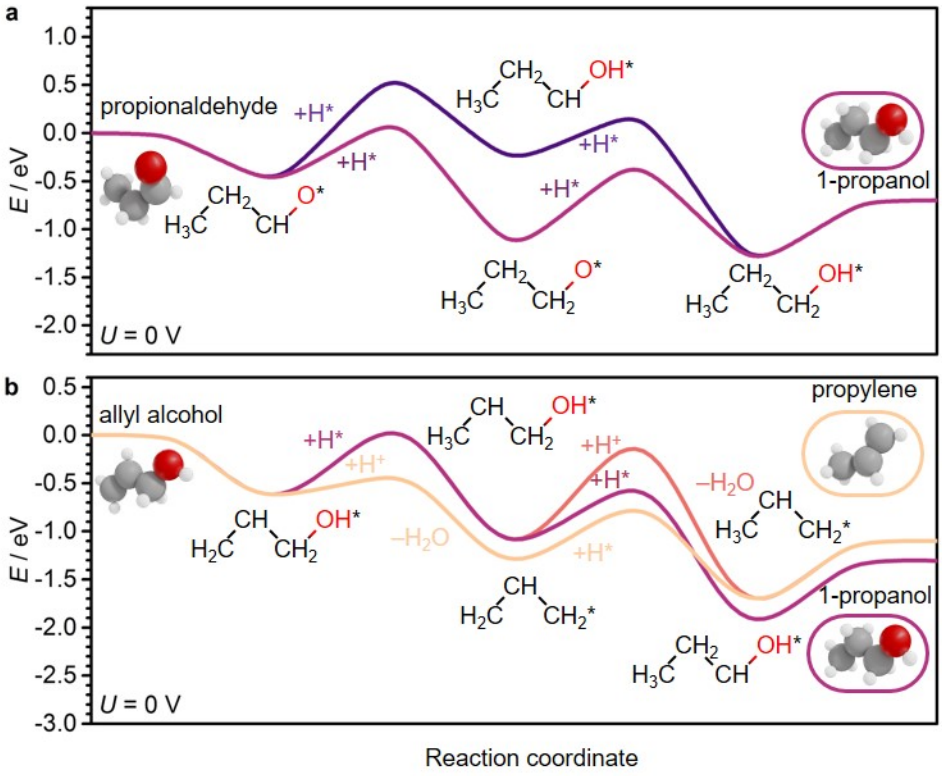

Figure S15. Energy profiles for electrocatalytic reduction of **a** propionaldehyde (CH_3CH_2CHO), and **b** allyl alcohol (CH_2CHCH_2OH) at 0.0 V *vs*. RHE on Cu(100), using H_2, CO_2, and H_2O as thermodynamic sinks, and shifting the energy reference to make (a) propionaldehyde and (b) allyl alcohol the zero. Lighter colours are associated with more favoured reaction paths.

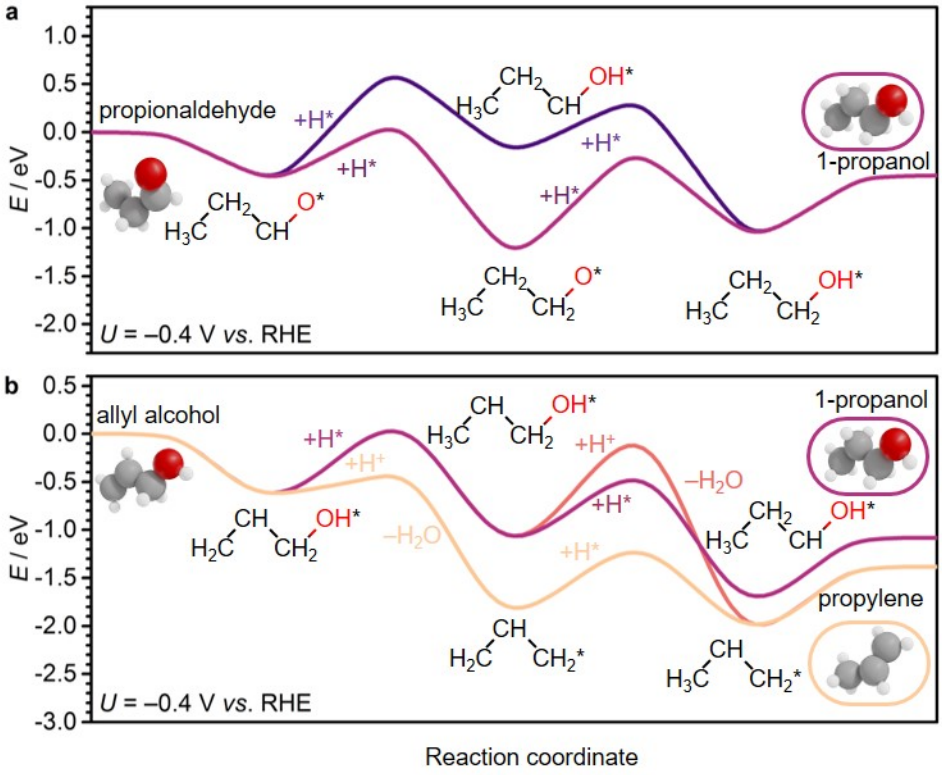

Figure S16. Energy profiles for electrocatalytic reduction of **a** propionaldehyde (CH_3CH_2CHO), and **b** allyl alcohol (CH_2CHCH_2OH) at –0.4 V *vs*. RHE on Cu(100), using H_2, CO_2, and H_2O as thermodynamic sinks, and shifting the energy reference to make (a) propionaldehyde and (b) allyl alcohol the zero. Lighter colours are associated with more favoured reaction paths.

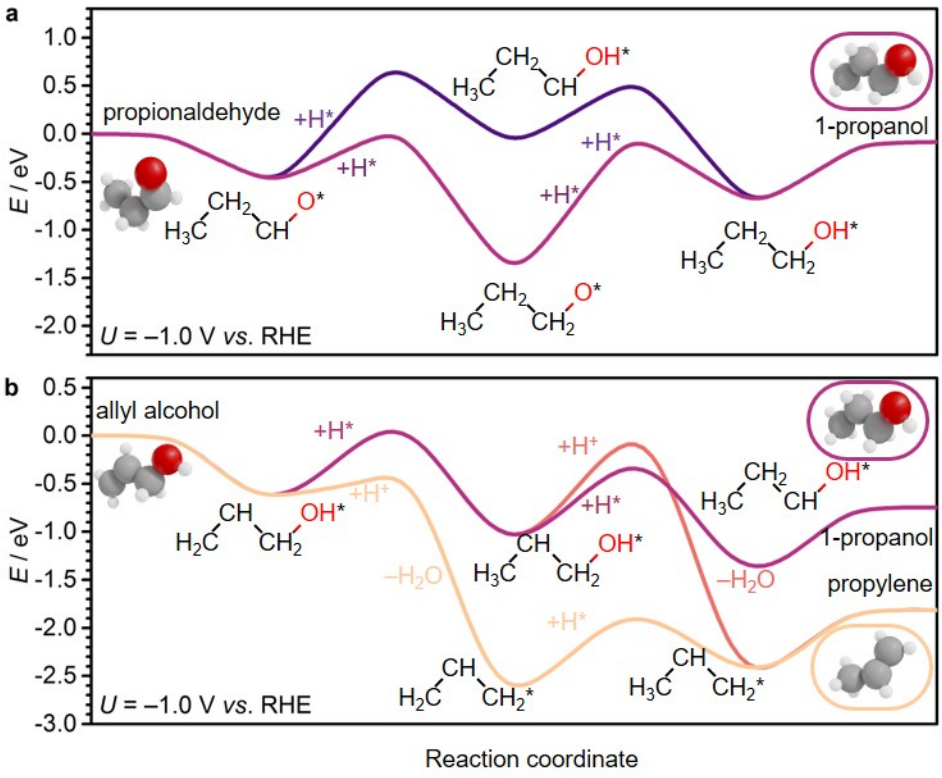

Figure S17. Energy profiles for electrocatalytic reduction of **a** propionaldehyde (CH_3CH_2CHO), and **b** allyl alcohol (CH_2CHCH_2OH) at –1.0 V *vs*. RHE on Cu(100) using H_2, CO_2, and H_2O as thermodynamic sinks, and shifting the energy reference to make (a) propionaldehyde and (b) allyl alcohol the zero. Lighter colours are associated with more favoured reaction paths.

SUPPLEMENTARY TABLES

Table S1. Reaction enthalpies from CO_2 and H_2 to H_2O(g) and relevant C_2–C_3 products[39]. A more negative enthalpy indicates a more favourable formation of the product from CO_2 and H_2.

Product	Δ*H* / eV
Ethylene	–1.32
Ethanol	–1.79
Propylene	–2.59
1-Propanol	–2.95
2-Propanol	–3.12

Table S2. Production rates (*r*), Faradaic efficiencies (*FE*) and geometric partial current densities (*j*) of products detected from the electrolysis of CO_2 (C_1 reagent) on OD-Cu in 0.1 M potassium bicarbonate at −0.95 V *vs*. RHE for 60 min. The values shown are an average taken from three experiments, with their standard deviations given in the brackets.

Products	*r* / μmol cm^{-2} h^{-1}	*FE* / %	*j* / mA cm^{-2}
Hydrogen	5710 (506)	37.4 (3.2)	−5.3 (1.3)
Carbon monoxide	182 (15)	1.17 (0.08)	−0.17 (0.02)
Methane	47.5 (8.5) [A]	1.3 (0.2)	−0.19 (0.03)
Ethylene	819 (78)	30.5 (2.6)	−4.4 (0.4)
Ethane	-	-	-
Propylene	-	-	-
Propane	-	-	-
Methanol	- [A]	-	-
Formate	1000 (97)	6.4 (2.0)	−0.92 (0.28)
Ethanol	326 (28)	12.5 (1.0)	−1.79 (0.16)
Acetaldehyde	18.8 (3.1)	0.61 (0.10)	−0.09 (0.02)
Acetate	32.9 (7.1)	0.85 (0.24)	−0.12 (0.04)
1-Propanol	75.8 (16.3)	4.4 (1.1)	−0.63 (0.13)
Propionaldehyde	20.3 (1.4)	1.04 (0.05)	−0.15 (0.10)
Acetone	3.2 (1.0)	0.16 (0.05)	−0.03 (0.01)
Allyl alcohol	25.2 (3.9)	1.2 (0.2)	−0.18 (0.06)
1-Butanol	-	-	-

[–] Product not detected.

[A] Low rates to CH_4 and CH_3OH hint low coverages for their precursors: CHOH, CH_2O, CH_2OH, CH_3O and CH_x.

Table S3. Faradaic efficiencies (*FE*) of products from the electrolysis of 50 mM formaldehyde + 50 mM acetaldehyde on OD-Cu in 0.1 M potassium phosphate buffer (pH 7) at different potentials for 60 min. The values shown are an average taken from three experiments.

Relevant Products	Applied potential / V *vs.* RHE			
	−0.80	−0.90	−1.00	−1.10
Hydrogen	25.8	36.9	64.9	75.3
Methane	Not detected	0.005	0.020	0.01
Ethylene	Not detected	Not detected	0.004	Not detected
Ethane	Not detected	0.007	0.06	0.002
Propylene	Not detected	Trace	0.005	0.0003
Propane	Not detected	Not detected	Trace	Not detected
Methanol	26.3	24.2	13.0	6.6
Ethanol	43.6	36.3	23.1	9.8
Allyl alcohol	Not detected	Not detected	0.0030	Not detected
1-Butanol	Not detected	0.006	0.025	0.010
Total	*95.7*	*97.5*	*101.1*	*91.8*
Total current density / mA cm^{-2}	−25.89	-36.0	−61.9	−188

Table S4. Production rates, in µmol cm^{-2} h^{-1}, of liquid products formed at open circuit potential (OCP) and at −0.4 V *vs*. RHE on OD-Cu in 0.1 M potassium hydroxide for 90 min. Production rates in µmol cm^{-2} h^{-1} of liquid and gaseous products detected from the electrolysis of CO or formaldehyde (50 mM) at –1.0 V *vs*. RHE on OD-Cu in 0.1 M potassium phosphate buffer (pH 7) for 60 min. Standard deviations are given in the brackets.

	Carbon monoxide			Formaldehyde
Relevant products	OCP	–0.4 V *vs*. RHE	–1.0 V *vs*. RHE	–1.0 V *vs*. RHE
Hydrogen	–	–	30468 (5840)	50490 (1888)
Formate	1.61	0.13	–	–
Methane	–	–[A]	34.9 (5.0)	16.2 (0.5)
Methanol	–	–[A]	4.6 (0.4)	8483 (529)
Ethylene	–	–	70.9 (15.8)	–
Ethane	–	–	0.15 (0.06)	–
Ethanol	0.01	0.22	26.5 (4.8)	–
Acetate	0.19	0.30	–	–
Acetaldehyde	3.16	trace	–	–
Propylene	–	–	–	–
Propionaldehyde	0.01	–	–	–
Allyl alcohol	–	–	2.1 (0.4)	–
1-Propanol	0.01	0.02	2.2 (0.4)	–

– Product not detected or process not applicable.

[A] Low rates to CH_4 and CH_3OH hint low coverages for their precursors: CHOH, CH_2O, CH_2OH, CH_3O and CH_x.

Table S5. Production rates (*r*) of products detected from the electrolysis of 50 mM acetaldehyde on OD-Cu in 0.1 M potassium phosphate buffer (pH 7) at −1.0 V *vs*. RHE for 60 min. The values shown are an average taken from three experiments, with their standard deviations given in the brackets.

Relevant Products	*r* / μmol cm^{-2} h^{-1}
Hydrogen	16937 (1888)
Methane	–
Ethylene	34.3 (4.1)
Ethane	195 (27)
Propylene	–
Methanol	–
Ethanol	13339 (962)
1-Propanol	–

– Product not detected or process not applicable.

Table S6. Production rates (*r*) of products detected from the electrolysis of CO (C_1 reagent) with 50 mM acetaldehyde (C_2 reagent) on OD-Cu in 0.1 M potassium phosphate buffer (pH 7) at −1.0 V *vs*. RHE for 60 min. The values shown are an average taken from three experiments, with their standard deviations given in the brackets.

Relevant Products	*r* / μmol cm^{-2} h^{-1}
Hydrogen	15189 (5911)
Methane	17.0 (4.6)
Ethylene	105 (8)
Ethane	0.26 (0.03)
Propylene	Trace
Methanol	–
Ethanol	9842 (2578)
1-Propanol	12.1 (3.8)
1-Butanol	0.4 (0.1)

– Product not detected or process not applicable.

Table S7. Production rates (*r*), Faradaic efficiencies (*FE*) and geometric partial current densities (*j*) of products detected from the electrolysis of 50 mM formaldehyde (C_1 reagent) and 50 mM acetaldehyde (C_2 reagent) on OD-Cu in 0.1 M potassium phosphate buffer (pH 7) at −1.0 V *vs*. RHE for 60 min. The values shown are an average taken from three experiments, with their standard deviations given in the brackets. We note that 1-propanol and acetone were not detected by headspace GC, while propane was qualitatively detected by GC. Results from control electrolysis experiments of formaldehyde (**Table S4**) or acetaldehyde (**Table S5**) allowed us to conclude that C_1 products originated from formaldehyde, C_2 and C_4 products from acetaldehyde, and C_3 products from the combination of both reactants. The *FE* and *j* values were calculated based on the number of electrons transferred from the respectively elucidated reactants.

Relevant Products	*r* / μmol cm^{-2} h^{-1}	*FE* / %	*j* / mA cm^{-2}
Hydrogen	39963 (2732)	64.9 (0.6)	–40.2 (2.7)
Methane	6.4 (0.4)	0.020 (0.001)	–0.0120 (0.0001)
Ethylene	2.9 (0.3)	0.004 (0.001)	–0.003 (0.001)
Ethane	20.4 (1.6)	0.06 (0.01)	–0.037 (0.009)
Propylene	1.4 (0.6)	0.005 (0.001)	–0.003 (0.001)
Propane	Trace	Trace	Trace
Methanol	8969 (611)	13.0 (1.6)	–8.0 (0.5)
Ethanol	16005 (752)	23.1 (0.3)	–14.3 (0.7)
Allyl alcohol	2.0 (0.4)	0.0030 (0.0004)	–0.0020 (0.0004)
1-Butanol	8.8 (0.5)	0.025 (1.5×10^{-7})	–0.016 (0.001)

Table S8. Production rates, in μmol cm^{-2} h^{-1}, of products formed under open circuit in 0.1 M potassium hydroxide in the presence of OD-Cu for 90 min upon bubbling carbon monoxide as C_1 reagent in the presence of C_2 reagents. Oxalate cannot be detected by ^{1}H NMR. Methanol and propanol were not detected by ^{1}H NMR. Propylene was not detected by headspace GC-MS.

Relevant products	C_2 reagents (50 mM)				
	Glyoxal	Ethylene glycol	Oxalate	Acetate	Ethanol
Glyoxal	–	0.12	–	–	2.22
Ethylene glycol	23.58	–	0.63	7.24	–
Acetate	0.13	0.05	32.57	–	0.05
Ethanol	–	1.04	–	0.12	–
Formate	3.06	0.67	1.09	1.35	1.36
Acetaldehyde	0.11	–	–	–	–

– Product not detected or process not applicable.

Table S9. Production rates, in μmol cm^{-2} h^{-1}, of products formed at −0.4 V *vs*. RHE on OD-Cu in 0.1 M potassium hydroxide for 90 min upon bubbling carbon monoxide as C_1 reagent in the presence of C_2 reagents. Oxalate cannot be detected by ^{1}H NMR. Propylene was not detected by headspace GC-MS.

Relevant products	C_2 reagents (50 mM)				
	Glyoxal	Ethylene glycol	Oxalate	Acetate	Ethanol
Glyoxal	–	0.22	5.83	0.14	–
Ethylene glycol	27.86	–	0.49	0.09	–
Acetate	4.53	0.45	0.26	–	2.10
Ethanol	0.89	1.40	0.34	0.21	–
Methanol	0.05	0.07	–	0.03	0.03
Formate	3.16	1.44	1.08	1.04	1.97
Acetaldehyde	0.13	–	–	–	–
1-Propanol	0.15	0.25	0.22	0.12	0.12

– Product not detected or process not applicable.

Table S10. Production rates, in μmol cm^{-2} h^{-1}, of products formed under open circuit in 0.1 M potassium hydroxide in the presence of OD-Cu for 90 min upon addition of formaldehyde (50 mM) as C_1 reagent in the presence of C_2 reagents. Oxalate cannot be detected by ^{1}H NMR. Propylene was not detected by headspace GC-MS.

Relevant products	C_2 reagents (50 mM)				
	Glyoxal	Ethylene glycol	Oxalate	Acetate	Ethanol
Glyoxal	–	–	0.40	0.37	0.25
Ethylene glycol	29.17	–	0.45	0.41	–
Acetate	0.28	0.46	0.20	–	0.16
Ethanol	0.09	–	0.13	0.00	–
Methanol	90.20	171.96	74.43	139.17	104.75
Formate	13.12	89.25	7.36	79.12	37.55
Acetaldehyde	0.20	–	0.38	–	–
1-Propanol	0.01	–	0.10	–	–

– Product not detected or process not applicable.

Table S11. Production rates, in μmol cm^{-2} h^{-1}, of products formed at −0.4 V *vs*. RHE on OD-Cu in 0.1 M potassium hydroxide for 90 min upon addition of formaldehyde (50 mM) as C_1 reagent in the presence of C_2 reagents. Oxalate cannot be detected by ^{1}H NMR. 1-Propanol was not detected by ^{1}H NMR. Propylene was not detected by headspace GC-MS.

Relevant products	C_2 reagents (50 mM)				
	Glyoxal	Ethylene glycol	Oxalate	Acetate	Ethanol
Glyoxal	–	–	0.38	0.36	0.37
Ethylene glycol	20.47	–	0.33	0.62	–
Acetate	0.17	1.21	0.24	–	0.22
Ethanol	0.10	–	0.09	–	–
Methanol	376.78	123.83	212.24	176.96	207.21
Formate	12.20	148.57	51.46	30.49	23.05
Acetaldehyde	0.14	–	–	–	–

– Product not detected or process not applicable.

Table S12. Production rates, in μmol cm^{-2} h^{-1}, of products formed under open circuit in 0.1 M potassium hydroxide in the presence of OD-Cu for 90 min upon addition of methanol (50 mM) as C_1 reagent in the presence of C_2 reagents. Oxalate cannot be detected by ^1H NMR. Propylene was not detected by headspace GC-MS.

Relevant products	C_2 reagents (50 mM)				
	Glyoxal	Ethylene glycol	Oxalate	Acetate	Ethanol
Glyoxal	–	–	1.69	–	–
Ethylene glycol	39.61	–	0.10	–	–
Acetate	0.25	0.07	0.09	–	0.05
Ethanol	0.11	–	0.05	0.03	–
Formate	4.83	–	0.08	–	–
Acetaldehyde	0.22	–	0.39	–	–
1-Propanol	0.15	–	0.10	0.01	–

– Product not detected or process not applicable.

Table S13. Production rates, in μmol cm^{-2} h^{-1}, of products formed on OD-Cu at −0.4 V *vs*. RHE in 0.1 M potassium hydroxide for 90 min upon addition of methanol (50 mM) as C_1 reagent in the presence of C_2 reagents. Oxalate cannot be detected by ^1H NMR. Propylene was not detected by headspace GC-MS.

Relevant products	C_2 reagents (50 mM)				
	Glyoxal	Ethylene glycol	Oxalate	Acetate	Ethanol
Glyoxal	–	–	0.04	–	–
Ethylene glycol	26.44	–	–	–	–
Acetate	0.12	0.15	0.05	–	0.07
Ethanol	0.08	–	0.01	–	–
Formate	2.35	0.34	0.16	0.05	0.25
Acetaldehyde	0.14	–	0.25	–	–
1-Propanol	0.08	–	0.09	–	–

– Product not detected or process not applicable.

Table S14. Concentrations and resulting background production rates of relevant impurities found in 50 mM solutions prepared with commercial glyoxal and sodium oxalate used for experiments reflected in **Tables S8**-**S13**.

	Glyoxal	Oxalate	Glyoxal	Oxalate
Relevant products	C / mM	C / mM	r / μmol cm^{-2} h^{-1}	r / μmol cm^{-2} h^{-1}
Ethylene glycol	3.830	0.000	41.69	0.00
Acetate	0.075	0.070	0.82	0.76
Ethanol	0.020	–	0.22	–
Methanol	–	–	–	–
Formate	0.330	0.075	3.59	0.82
Acetaldehyde	0.020	–	0.22	–
1-Propanol	–	–	–	–

– Product not detected or process not applicable.

Table S15. Values of α and β in **Eq. S5** used to approximate the energies of transition states, E_{TS}, for O–H and C–H hydrogenations. Taken from Supplementary Tables 8-9 in Ref. [15]. We selected the LSR with the lowest MAE on Cu: BEP for O–H and C–H breakings. Parameters for C–C, C–O, and C–OH, although not used in this work, are also shown for completeness. (1–α) values that describe bond formations are shown as a reference.

Bond breaking	O–H	C–H	C–C	C–O	C–OH
α / –	0.39	0.63	1.00	1.00	1.00
(1–α) / –	0.61	0.37	0.00	0.00	0.00
β / eV	0.89	0.81	0.64	1.24	1.48

BEP: Brønsted-Evans-Polanyi, FSS: Final-State Scaling. MAE: Mean Absolute Error.

Table S16. Reaction energies, ΔE (**Eq. S3**) in eV, for C_1–C_2 couplings. Exothermic values indicate larger thermodynamic driving forces to the corresponding C_3 products. The (–) marks the direction in which the C–C bond is formed. Void boxes indicate unstable C_3 species. Thicker lines cluster C_1 and C_2.

	–C	–CH	–CH_2	–CH_3	–CO	–COH	–CHO	–CHOH	–CH_2O	–CH_2OH
CC–	-0.66	-0.83	-1.06	-1.08	0.04	-0.70	-1.15	-1.16	-0.77	-1.27
CHC–	-0.87	-0.38	-1.00	-0.94	0.12	-0.06	-0.93	-0.95	0.33	0.18
CH_2C–	-0.82	-0.72	-1.05	-0.73	-0.17	-0.67	-0.68	-0.49	-0.46	-0.62
CH_3C–	-1.14	-0.96	-1.03	-0.27	-0.32	-1.12	-1.38	-1.31	0.14	-0.54
CCH–	-0.21	-0.32	-0.87	-0.85	0.40	0.01	-1.15	-1.21	-0.72	-0.92
CHCH–	-0.53	-0.45	-1.01	-0.61	0.08	-0.57	-0.84	-0.87	-0.25	-0.79
CH_2CH–	-0.93	-0.87	-1.50	-1.17	0.25	-0.41	-1.52	-1.57	-1.14	-1.09
CH_3CH–	-1.56	-1.11	-1.82	-1.07	-0.36	-1.33	-1.98	-1.88	-1.16	-1.46
CCH_2–	0.49		-0.51	-0.88		0.54	-0.74	-0.44	-0.35	-1.03
$CHCH_2$–		0.38	-0.42	-0.42	0.52	0.10	-0.38	-0.19	-0.24	-0.60
CH_2CH_2–	-0.13	0.30	-0.48	-0.49	0.38	-0.02	-0.41	-0.32	-0.33	-0.62
CH_3CH_2–	-1.18	-0.38	-1.17	-1.36	0.91	-0.60	-1.15	-1.05	-1.36	-1.59
COC–	0.24	0.36	-0.21	-0.06	1.53	0.37	-0.25	0.35	0.48	0.28
COHC–	-0.77	-0.09	-0.99	-1.14	0.10	0.30	-0.50	-1.02	-0.66	-1.07
CHOC–	-0.99	-0.73	-0.77	-1.17	-0.30	-0.28	-1.67	-1.15	-0.51	-1.32
CHOHC–	-0.43	-0.19	-0.01	-0.54	0.87	-0.23	-0.59	0.50	-0.45	-0.17
CH_2OC–	-1.68	-0.54	-1.61	-0.71	-0.64	-1.50	-1.58	-2.08		-1.24
CH_2OHC–	-1.16	0.32	-0.75	-0.37	0.18	-0.90	-1.37	-0.78	-0.22	0.06
COCH–	-0.16	-0.27	-0.25	-0.21	0.92	1.01	0.17	-0.77	0.42	0.13
COHCH–	-0.01	-0.38	-0.38	-0.65	1.55	1.26		-0.34	0.00	-0.40
CHOCH–	-0.78	-0.26	-1.09	-0.91	1.10		-0.61	-0.68	-0.49	-0.76
CHOHCH–	-0.89	-0.34	-1.19	-0.85	0.11	0.01	-0.73	-0.89	-0.41	-0.65
CH_2OCH–	-1.87	-1.18	-2.22	-1.59	-0.16	-1.12	-2.00	-1.88	-1.37	-1.56
CH_2OHCH–	-1.38	-1.04	-1.49	-1.21	0.23	-0.84	-1.59	-1.44	-0.88	-1.11
$COCH_2$–		-0.16	-1.02	0.18	0.52	0.04	-0.37	-0.49	0.79	0.33
$COHCH_2$–	0.42	0.32	-0.52	-0.42	0.94	0.57	0.23	-0.09	0.03	-0.43
$CHOCH_2$–	-0.14	0.55	-0.20	-0.26	1.24	0.94	0.40	0.36	-0.03	-0.18
$CHOHCH_2$–	-0.01	0.59	-0.26	-0.31	0.97	0.47	0.21	-0.17	0.58	0.53
CH_2OCH_2–	-0.56	-0.11	-0.92	-1.27	1.60	-0.06	-0.83	-0.06	-1.02	-1.15
CH_2OHCH_2–	-1.00	-0.23	-0.97	-1.27	1.38	-0.28	-0.74	0.12	-0.91	-1.24

Continues on next page.

Table S16. Continues from the previous page.

	–C	–CH	–CH_2	–CH_3	–CO	–COH	–CHO	–CHOH	–CH_2O	–CH_2OH
CCO–			0.51	0.18		1.63	0.79	0.95	0.66	0.30
CHCO–		0.67	-0.26	-0.82		1.72	-0.28	-0.16	0.08	-0.61
CH_2CO–	-0.47	-0.44	-1.87	-1.46	0.04	-0.47	-1.19	-1.39	-0.82	-1.28
CH_3CO–	-0.91	-1.11	-1.57	-0.82	0.32	-0.86	-1.06	-1.13	-0.57	-0.69
CCOH–			-0.79	-0.93		0.14	-0.85	-0.77	-0.59	-0.94
CHCOH–		-0.36	-0.33	-0.57	1.49	-0.16	-0.57	-0.06	0.16	-0.58
CH_2COH–	-0.60	-0.15	-1.39	-0.91	0.21	-0.35	-0.95	-1.20	-1.14	-0.99
CH_3COH–	-1.48	-1.13	-1.65	-0.46	0.14	-0.69	-1.38	-1.46	-0.34	-0.60
CCHO–				0.28		1.12	0.80			0.32
CHCHO–				0.55		0.97	0.46			0.11
CH_2CHO–			0.08	-0.06		0.79	0.31	0.30	0.38	0.10
CH_3CHO–	0.05	0.14	-0.98	-1.12	-0.01	-0.25	-0.67	-0.70	-0.64	-1.12
CCHOH–				-0.10			0.20		0.16	-0.06
CHCHOH–		1.06	0.01	-0.11	1.28	0.31	0.70	-0.19	0.21	-0.13
CH_2CHOH–		0.41	-0.42	-0.45	0.67	0.23	-0.11	-0.30	-0.07	-0.56
CH_3CHOH–	-0.80	-0.38	-1.11	-1.18	-0.05	-0.50	-0.69	-0.90	-0.96	-1.26
COCO–			-1.09	-0.70	0.83	-0.86	-0.69	-1.22	-0.34	-0.96
COHCO–	0.08	0.97	-1.04	-1.32	-0.30	-1.19	-0.66	-1.20	0.04	-0.62
CHOCO–	-0.43	-0.70	-1.43	-1.19	0.19	-0.33	-1.63	-1.79	-1.10	-1.62
CHOHCO–	-0.64	-0.95	-2.00	-1.63	-0.71	-1.24	-2.16	-2.03	-2.07	-1.71
CH_2OCO–	-0.36	-0.13	-0.85	-0.49	0.75	0.57	-0.89	-1.50	-0.16	-0.44
CH_2OHCO–	-0.78	-0.89	-1.38	-0.68	0.06	-0.15	-1.47	-1.19	-0.50	-0.94
COCOH–		0.21	-1.26	-0.58	-0.48	-1.36	-0.40	-1.64	-0.16	-0.41
COHCOH–	0.28	-0.02	-0.39	0.01	0.06	-0.73	-0.67	-0.47	-0.18	-0.17
CHOCOH–	-0.69	-0.42	-0.98	-0.67	1.04	-0.65	-0.94	-1.03	-0.80	-1.05
CHOHCOH–	-0.62	0.07	-1.25	-0.76	-0.22	-0.47	-1.05	-1.13	-1.28	-1.04
CH_2OCOH–	-1.10	-0.36	-1.84	-0.30	0.60	-0.83	-1.47	-1.94		
CH_2OHCOH–	-1.51	-1.17	-1.76	-0.63	0.29	-0.89	-1.79	-1.76		-0.75
COCHO–				-0.95	0.35			-0.77	-0.61	-1.26
COHCHO–	1.06	0.73	0.05	-0.08		0.59	0.31	-0.16		-0.67
CHOCHO–	1.10	0.59	-0.07	-0.13		0.68	0.08	-0.14	-0.06	-0.57
CHOHCHO–			-0.18	-0.26	0.60	0.11	-0.24	-0.02	-0.39	
CH_2OCHO–			-0.47	-0.57	0.40		-0.53	-0.75	-0.17	-0.74
CH_2OHCHO–	0.06	-0.32	-0.83	-1.14	-0.34	-0.86	-1.13		-0.83	-1.63
COCHOH–		-0.40	-1.40	-1.46	-0.41	-0.81		-1.49	-1.41	-1.72
COHCHOH–		0.10	-0.37	-0.44	0.65	-0.02	-0.14	-0.44	-0.15	-0.69
CHOCHOH–	-0.17	0.77	-0.44	-0.36		0.14	-0.08	-0.59	-0.59	-0.63
CHOHCHOH–		-0.03	-0.53	-0.48	0.35	-0.07	-0.50	-0.57	-0.52	-0.71
CH_2OCHOH–	-0.66	-0.18	-0.86	-1.08	-0.13	-0.33	-1.05	-1.07	-1.04	-0.97
$CH_2OHCHOH$–	-0.51	-0.14	-0.97	-1.01	-0.06	-0.49	-0.71	-0.88	-0.59	-1.20

Table S17. Activation energies (E_a) in eV, for the different C_1–C_2 couplings. Zero values indicate barrierless reactions. For reaction marked with an asterisk (*), the minimum-energy path was not fully converged, thus the table with the maximum energy descent was selected. The connecting point between the two fragments is shown by (–) marks the direction. Void boxes denote not located transition states.

	–C	–CH	–CH_2	–CH_3	–CO	–COH	–CHO	–CHOH	–CH_2O	–CH_2OH
CC–	1.02	1.45	1.46	1.33	0.82	0.95	0.51	0.38	0.24	1.23
CHC–	1.10	0.62	0.85	0.81	0.99		0.43	0.91	0.81	2.00
CH_2C–	1.82	1.83	1.41	1.25	1.10	1.31	0.60	0.48	0.76	1.40
CH_3C–		1.31	0.38	1.00	0.96	0.88	*0.75			0.92
CCH–	0.57	*0.85	0.50	1.82	1.51	1.13	0.41	*1.93	0.59	1.36
CHCH–	*0.69	0.94	0.70	*2.37	1.23	1.15	0.23	1.46	0.59	*2.41
CH_2CH–	1.00	0.83	1.42	*0.96	0.76	1.14	0.08	*0.45	0.72	*2.00
CH_3CH–	1.34	*0.87	*0.11	0.41	0.62	*1.12	0.19	0.00	0.68	*1.60
CCH_2–	1.00			1.33		1.24	1.53	0.36	*0.60	*0.86
$CHCH_2$–		1.81	1.08	1.64	0.98	1.56	0.24	0.80	0.53	*0.35
CH_2CH_2–		1.45	1.19	1.73	1.11	1.53	1.61	1.05	1.22	2.02
CH_3CH_2–	0.98	0.75	0.68	2.70	2.15	1.21		0.26	1.06	*1.11
COC–	1.38	1.34	1.54	2.09	2.07	1.73	1.81	0.74	0.98	1.58
COHC–	1.22	1.08	0.66	0.94	1.42		0.61	0.82	*0.38	0.98
CHOC–	0.98	0.63	0.52	*0.95	1.73	1.62	0.35	0.34	0.60	0.68
CHOHC–	1.24	1.34		1.62	1.35	1.71	0.80	*1.84	0.87	1.05
CH_2OC–			0.39		1.09	*1.10	0.50	0.43		0.78
CH_2OHC–	0.91	1.53	0.80	1.09	1.43		0.44	0.99	0.77	1.06
COCH–	2.47		1.60	1.43	1.76	1.48	1.05	2.09	0.68	*1.84
COHCH–	1.28		1.89	*2.79	2.12	0.50		*1.35	*1.09	1.24
CHOCH–	0.63	1.42	1.25	0.87	1.04		*3.12	0.70	0.71	1.39
CHOHCH–	*1.40	1.16	*0.68	1.53	1.14		0.65	0.78	0.81	*1.37
CH_2OCH–		1.36		0.00	1.09	*0.73	0.00	0.34	0.40	0.63
CH_2OHCH–	0.97	*0.87	*1.36	*0.56	*1.72	1.37	0.16	*2.34	0.82	*1.66
$COCH_2$–		1.48	0.86	2.37	0.65		0.78	0.84	*0.82	1.96
$COHCH_2$–	0.99	1.87	1.17	1.90	1.18	1.30	0.71	1.13	*0.62	*1.01
$CHOCH_2$–	2.37	1.52	1.24	2.24	1.59	1.57	*2.36	1.41	*1.04	*2.47
$CHOHCH_2$–	1.85	2.05	1.17	1.03	1.46		2.36	0.92	0.64	1.87
CH_2OCH_2–	*0.67	0.77	1.24	*2.18	*2.35	*1.43	*1.71	1.37	1.63	*1.57
CH_2OHCH_2–	*0.56	*1.15	1.39	*1.65	2.36	*1.37		2.32	1.06	*0.94

Continues on next page.

Table S17. Continues from the previous page.

	–C	–CH	–CH_2	–CH_3	–CO	–COH	–CHO	–CHOH	–CH_2O	–CH_2OH
CCO–			1.26	*1.60		1.87	1.56	*0.94	1.08	1.04
CHCO–		1.55	1.08	2.11			1.06	1.23	1.00	1.37
CH_2CO–	0.83	0.71		0.84	0.62	0.98	*0.00	*0.00	0.00	*0.42
CH_3CO–	*0.57	0.72	0.28	*1.74	*0.75	1.01	0.32	*0.73	*0.63	*1.55
CCOH–			1.53	*0.45			0.44	*0.25	*0.60	
CHCOH–		*0.96		3.09	2.62	0.68	*3.21	1.83	*1.41	*2.27
CH_2COH–	2.36	*1.42	1.12	1.88	*1.14	1.45	0.52	0.41		*0.41
CH_3COH–	*0.67	0.26	1.86	1.77	0.69	1.14	0.21	1.91	*0.35	*0.69
CCHO–						1.67	*0.71			*1.14
CHCHO–				2.15			0.91			*0.93
CH_2CHO–			1.24	1.48	2.05	1.96	0.97	1.24	1.16	1.47
CH_3CHO–	1.86	0.92	0.48	0.83	0.30	1.14	*1.25	0.58	0.50	*0.22
CCHOH–				2.02			1.06		0.59	*0.80
CHCHOH–		1.92	1.34	1.70	1.25		1.51		0.70	1.40
CH_2CHOH–		1.68	1.22	1.50	0.88	1.58	1.03	0.97	0.92	1.64
CH_3CHOH–	0.71	1.10	1.15	*1.15	0.99	1.45	1.18	1.28	*0.74	*1.29
COCO–				*1.41	0.92	0.96	0.73	0.41	0.79	*1.49
COHCO–	1.97	1.21	0.40	1.81	0.79		1.15	0.52		0.25
CHOCO–	2.24	1.02	*0.76	1.04	*0.95	1.23	0.29	*3.09	*0.70	*0.16
CHOHCO–	*0.82	0.14	*0.00	*0.14	0.03	0.53	*1.01	0.00	0.00	*0.70
CH_2OCO–	0.55		1.04	*1.91	1.41	1.51	*0.47	0.54	1.23	*1.36
CH_2OHCO–	1.69	0.84	*0.50	*1.65	*0.70		*0.13	*0.39	*1.44	*1.57
COCOH–		1.56	*0.05	0.55	0.96		1.29		0.76	1.65
COHCOH–		1.73	0.99	1.30	*1.07		*1.79	0.51	*1.77	*2.66
CHOCOH–	1.47	*0.93	1.32	1.82	3.31	*1.60	1.47	*1.91	1.40	*0.89
CHOHCOH–	*1.06	1.28	0.64	2.97	0.91	1.31	*0.54	0.81	*0.24	*1.76
CH_2OCOH–	*1.85	*1.45		*0.61	1.84		0.54			
CH_2OHCOH–	0.72	*0.15		*2.85	1.37	*0.93	*0.01	*0.00		*1.86
COCHO–				0.91	0.78			0.72	0.42	*0.01
COHCHO–	1.07		1.26	1.56		1.42				*0.48
CHOCHO–	*0.96	1.46	0.78	*1.64		1.65	*0.97	0.56	*0.36	1.32
CHOHCHO–			1.10	1.31	1.16		0.78	0.87	0.76	
CH_2OCHO–			0.72	1.40	0.80		*1.86	0.47	0.93	*1.03
CH_2OHCHO–	*0.64	*0.74	0.37	*0.77	*0.41	*0.97	0.47		*0.13	*0.65
COCHOH–		0.47	0.24	0.91	0.00	*0.84		0.00	0.00	*0.01
COHCHOH–			1.03	1.72	*0.33	1.29		0.56	*0.45	1.18
CHOCHOH–	1.62	1.33	0.68	1.47		1.25	0.61	*0.40	*0.51	*2.03
CHOHCHOH–			1.12	1.58	1.14	1.65	*0.79	0.93	0.85	*2.07
CH_2OCHOH–	0.71	1.27	0.96	*1.82	0.97		*0.22			*0.99
$CH_2OHCHOH$–	*2.41	1.56	1.19	*1.85	*1.21	1.89	*2.33	*1.60	*1.80	*1.60

Table S18. Bader charge differences upon reaction, $\Delta\Delta Q_B$ (in $|e^-|$, **Eq. S5** in Main Text), for C_1–C_2 couplings. Negative values indicate that the C_3 products have more electronic density than the combined C_1–C_2 reactants and thus the net reaction is promoted under reductive potentials. The (−) marks the direction in which the C–C bond is formed. Void boxes indicate unstable C_3 species. Thicker lines cluster C_1 and C_2.

	–C	–CH	–CH_2	–CH_3	–CO	–COH	–CHO	–CHOH	–CH_2O	–CH_2OH
CC–	0.60	0.72	0.91	0.89	0.47	0.55	0.65	0.60	0.63	0.62
CHC–	0.48	0.75	0.86	0.33	0.31	0.78	0.35	0.32	0.77	0.87
CH_2C–	0.87	1.05	0.67	0.60	0.30	0.78	0.64	0.87	0.46	0.52
CH_3C–	1.18	0.86	0.93	0.70	0.55	0.64	0.37	0.59	1.02	0.54
CCH–	0.25	0.27	0.53	0.38	0.38	0.53	0.10	0.29	0.21	0.23
CHCH–	0.45	0.72	0.72	0.65	0.24	0.63	0.29	0.28	0.48	0.50
CH_2CH–	0.60	0.61	0.71	0.71	0.50	0.53	0.30	0.35	0.48	0.61
CH_3CH–	0.90	0.99	1.16	0.63	0.12	0.70	0.51	0.80	0.45	0.51
CCH_2–	0.46		0.73	0.31		0.42	0.54	0.38	0.20	0.24
$CHCH_2$–		0.52	0.44	0.32	0.01	0.46	0.46	0.16	0.02	0.21
CH_2CH_2–	0.44	0.27	0.16	0.10	-0.31	0.21	0.25	-0.18	-0.05	-0.03
CH_3CH_2–	0.54	0.68	0.62	0.49	0.43	0.64	0.75	0.32	0.39	0.45
COC–	0.87	0.95	0.75	0.66	1.05	0.84	0.77	0.95	0.50	0.52
COHC–	0.55	1.03	0.84	0.35	0.44	0.45	0.36	0.39	0.24	0.24
CHOC–	1.01	0.94	1.05	0.43	0.72	0.71	0.57	0.70	0.36	0.31
CHOHC–	0.92	0.88	1.23	0.62	0.86	0.71	0.66	0.83	0.49	0.50
CH_2OC–	0.97	1.35	0.85	1.07	0.44	0.58	0.34	0.51		0.45
CH_2OHC–	1.06	1.56	1.02	0.70	0.56	0.68	0.40	0.62	0.55	0.44
COCH–	0.79	0.47	0.84	0.00	0.25	0.76	0.91	0.19	0.61	0.64
COHCH–	0.97	0.90	0.90	0.62	0.80	0.85		0.90	0.41	0.54
CHOCH–	0.74	0.76	0.88	0.63	1.15		0.70	0.99	0.52	0.53
CHOHCH–	0.73	0.54	0.72	0.72	0.22	0.90	0.78	0.29	0.52	0.56
CH_2OCH–	0.65	0.75	0.86	0.38	0.65	0.41	0.31	0.52	0.22	0.24
CH_2OHCH–	0.78	0.87	1.09	0.54	0.79	0.65	0.44	0.67	0.35	0.40
$COCH_2$–		0.02	-0.14	0.07	-0.55	-0.05	-0.05	-0.48	-0.03	-0.11
$COHCH_2$–	0.56	0.73	0.64	0.55	0.22	0.49	0.53	0.16	0.58	0.37
$CHOCH_2$–	0.84	0.88	0.85	0.82	0.37	0.69	0.98	0.51	0.68	0.75
$CHOHCH_2$–	0.39	0.30	0.12	0.10	-0.35	0.03	0.23	-0.31	0.49	0.32
CH_2OCH_2–	0.59	0.52	0.63	0.54	0.48	0.82	0.76	0.86	0.39	0.46
CH_2OHCH_2–	0.58	0.68	0.61	0.56	0.35	0.57	0.79	0.65	0.42	0.42

Continues on next page.

Table S18. Continues from the previous page.

	–C	–CH	–CH_2	–CH_3	–CO	–COH	–CHO	–CHOH	–CH_2O	–CH_2OH
CCO–			0.16	0.13		0.33	0.24	0.23	0.05	0.07
CHCO–		0.16	0.05	-0.09		-0.02	-0.07	-0.06	-0.31	-0.27
CH_2CO–	-0.41	-0.28	-0.29	-0.32	-0.65	-0.29	-0.52	-0.67	-0.52	-0.40
CH_3CO–	0.45	0.46	0.56	0.74	0.12	0.24	0.02	0.16	0.54	0.63
CCOH–			0.52	0.43		0.53	0.34	0.24	0.25	0.20
CHCOH–		0.78	0.82	0.70	0.67	0.47	0.71	0.54	0.47	0.54
CH_2COH–	0.61	0.71	0.79	0.76	0.06	0.48	0.30	0.30	0.58	0.63
CH_3COH–	0.63	0.70	0.87	0.86	-0.19	0.36	0.22	0.36	0.22	0.73
CCHO–				0.19		0.35	0.29			0.01
CHCHO–				0.32		0.45	0.43			0.17
CH_2CHO–			0.16	0.08		0.31	0.22	-0.15	-0.12	-0.06
CH_3CHO–	-0.09	0.00	-0.08	-0.20	-0.46	0.01	0.02	-0.49	-0.34	-0.34
CCHOH–				0.22			0.35		0.08	0.06
CHCHOH–		0.39	0.28	0.24	-0.12	0.23	0.32	0.15	0.09	0.14
CH_2CHOH–		0.05	0.05	-0.03	-0.38	0.06	0.12	-0.33	-0.20	-0.14
CH_3CHOH–	0.46	0.61	0.57	0.52	0.09	0.56	0.47	0.15	0.33	0.37
COCO–			0.73	0.61	0.14	0.31	0.81	0.27	0.52	0.20
COHCO–	0.41	0.30	0.36	0.01	-0.41	0.16	-0.25	-0.02	-0.11	-0.26
CHOCO–	0.63	0.56	0.44	0.10	0.39	0.06	0.07	0.37	-0.09	-0.05
CHOHCO–	0.19	0.14	-0.14	-0.20	-0.58	-0.14	-0.06	-0.43	-0.35	-0.35
CH_2OCO–	0.38	0.27	0.39	0.57	0.05	0.14	-0.14	0.03	0.37	0.43
CH_2OHCO–	0.40	0.30	0.51	0.65	-0.27	-0.01	-0.11	0.02	0.43	0.50
COCOH–		0.95	0.45	0.09	-0.37	0.27	0.91	0.12	0.59	0.60
COHCOH–	0.91	0.65	0.77	0.54	0.16	0.65	0.64	0.62	0.37	0.39
CHOCOH–	0.98	1.14	0.85	0.65	1.07	0.89	0.69	0.97	0.50	0.49
CHOHCOH–	0.73	0.83	0.70	0.65	0.13	0.73	0.83	0.35	0.54	0.55
CH_2OCOH–	0.37	0.39	0.61	0.14	0.23	0.11	-0.02	0.17		
CH_2OHCOH–	0.65	0.79	1.00	0.98	0.57	0.46	0.31	0.51		0.86
COCHO–				0.24	0.10			0.06	0.14	0.09
COHCHO–	0.63	0.69	0.70	0.57		0.67	0.73	0.31		0.33
CHOCHO–	0.75	0.85	0.80	0.76		0.91	0.95	0.39	0.56	0.63
CHOHCHO–			0.31	0.14	-0.02	0.38	0.28	-0.05	0.06	
CH_2OCHO–			-0.20	-0.26	-0.48		-0.09	-0.48	-0.36	-0.36
CH_2OHCHO–	-0.16	-0.05	-0.12	-0.24	-0.51	-0.12	0.00		-0.34	-0.29
COCHOH–		0.05	0.01	-0.11	-0.42	-0.08		-0.38	-0.30	-0.37
COHCHOH–		0.52	0.59	0.49	0.05	0.35	0.64	0.15	0.53	0.35
CHOCHOH–	0.74	0.83	0.87	0.61		0.86	0.90	0.49	0.67	0.58
CHOHCHOH–		0.41	0.16	0.04	-0.29	0.12	0.24	-0.27	-0.11	-0.10
CH_2OCHOH–	0.44	0.57	0.51	0.45	0.02	0.72	0.63	0.11	0.25	0.37
$CH_2OHCHOH$–	0.41	0.61	0.56	0.47	-0.06	0.52	0.54	0.12	0.36	0.39

Table S19. Reaction and activation energies, ΔE and E_a, in eV, for crucial C_1–C_2 condensation reactions at U = 0.0 V *vs*. RHE found in **Table S17**. DFT values without solvation are indicated with "$_{DFT}$" subscript. Bader charge differences upon reaction, $\Delta\Delta Q_{B,\Delta E}$, and from the initial to the transition state, $\Delta\Delta Q_{B,Ea}$. Positive values indicate an increase in electronic density, thus the given step is promoted under reductive potentials. The labels to find the respective transition states in the ioChem-BD database are indicated[9,10]. Four substitution reactions were also considered, where CO or CHO replaces O or OH in a concerted step.

Reaction (top) Label ioChem-BD (bottom)	ΔE_{DFT} / eV	$E_{a,DFT}$ / eV	ΔE / eV	E_a / eV	$\Delta\Delta Q_{B,\Delta E}$ / e$^-$	$\Delta\Delta Q_{B,Ea}$ / e$^-$
COCO*+CO*→COCOCO*+* i202101+i101101-i303101+i000000	0.54	0.96	0.30	0.92	–0.14	–0.07
COCO*+CHO*→COCOCHO+* i202101+i111101-i313101+i000000	-0.75	0.73	-0.69	0.73	-0.81	–0.12
COCHO*+CO*→COCOCHO+* i212101+i101101-i313101+i000000	-0.10	0.81	0.18	0.78	-0.39	–0.02
CH_2CH*+CO*→CH_2CHCO*+* i230102+i101101-i331102+i000000	0.30	0.78	0.25	0.76	–0.50	–0.18
CH_2CH*+CHO*→CH_2CHCHO*+* i230102+i111101-i341104+i000000	–1.47	0.09	–1.52	0.08	–0.30	–0.90
CH_2CH*+CH_2O*→CH_2CHCH_2O*+* i230102+i121101-i351105+i000000	–1.11	0.71	–1.14	0.72	–0.48	–0.53
$CHCH_2$*+CH_2O*→$CHCH_2CH_2O$*+* i230102+i121101-i351106+i000000	–0.25	0.50	-0.24	0.53	–0.02	–0.46
CH_2CHO*+CO*→CH_2CHCO*+O* i231101+i101101-i331102+i001101	1.13	2.08	1.06	2.05	0.42	0.26
CH_2CHO*+CO*→$CH_2C(O)HCO$*+* i231101+i101101-i332202+i000000	1.04	1.88	1.24	1.78	–0.37	–0.08
CH_2CHO*+CHO*→CH_2CHCHO*+O* i231101+i111101-i341104+i001101	–0.64	0.95	–0.71	0.97	0.62	0.02
CH_3CH*+CHO*→CH_3CHCHO*+* i240101+i111101-i351102+i000000	–1.98	0.17	–1.98	0.19	–0.51	–0.29
CH_3CH*+CH_2O*→CH_3CHCH_2O*+* i240101+i121101-i361102+i000000	–1.15	0.68	–1.16	0.68	–0.45	–0.51
CH_2CH_2*+CO*→CH_2CH_2CO*+* i240102+i101101-i341102+i000000	0.39	1.06	0.38	1.11	0.31	0.10
CH_2CH_2*+CHO*→CH_2CH_2CHO*+* i240102+i111101-i351103+i000000	–0.36	1.63	–0.41	1.61	–0.25	–0.26
CH_2CH_2*+CH_2O*→$CH_2CH_2CH_2O$*+* i240102+i121101-i361103+i000000	–0.39	1.21	–0.33	1.22	0.05	–0.35
CH_2CHOH*+CO*→CH_2CHCO*+OH* i241103+i101101-i331102+i011101	0.30	0.86	0.32	0.88	0.53	0.48
CH_2CHOH*+CHO*→CH_2CHCHO*+OH* i241103+i111101-i341104+i011101	–1.47	0.97	–1.45	1.03	0.72	0.33
CH_3CH_2*+CH_2O*→$CH_3CH_2CH_2O$*+* i250101+i121101-i371101+i000000	–1.33	1.03	–1.36	1.06	0.39	0.05

Table S20. Reaction and activation energies, ΔE and E_a, in eV, for selected C–O(H) breaking reactions at U = 0.0 V *vs*. RHE. DFT values without solvation are indicated with "$_{DFT}$" subscript. Bader charge differences upon reaction, $\Delta\Delta Q_{B,\Delta E}$, and from the initial to the transition state, $\Delta Q_{B,Ea}$. Positive values indicate an increase in electronic density, thus the given step is promoted under reductive potentials. The labels to find the respective transition states in the ioChem-BD database are indicated[9,10].

Reaction (top) Label ioChem-BD (bottom)	ΔE_{DFT} / eV	$E_{a,DFT}$ / eV	ΔE / eV	E_a / eV	$\Delta\Delta Q_{B,\Delta E}$ / e$^-$	$\Delta\Delta Q_{B,Ea}$ / e$^-$
CH2CHCO*+*→ CH2CHC*+O* i331102+i000000-i330102+i001101	–0.07	1.58	–0.06	1.59	1.63	1.08
CH2CHCHO*+*→CH2CHCH*+O* i341104+i000000-i340104+i001101	0.52	2.07	0.53	2.08	1.03	0.45
CH2CHCOH*+*→CH2CHC*+OH* i34110a+i000000-i330102+i011101	–0.61	1.33	–0.54	1.42	0.91	0.49
CH3CHCHO*+*→CH3CHCH*+O* i351102+i000000-i350102+i001101	0.79	2.38	0.76	2.34	0.86	0.36
CH2CHCH2O*+*→CH2CHCH2*+O* i351105+i000000-i350105+i001101	–0.01	1.25	–0.03	1.26	0.76	0.34
CH2CHCHOH*+*→CH2CHCH*+OH* i35110a+i000000-i340104+i011101	–0.06	1.28	0.00	1.31	0.90	0.49
CH3CHCH2O*+*→CH3CHCH2*+O* i361102+i000000-i360102+i001101	–0.28	0.95	–0.33	0.95	0.28	0.07
CH3CHCHOH*+*→CH3CHCH*+OH* i361105+i000000-i350102+i011101	–0.02	1.58	0.07	1.64	0.97	0.45
CH2CHCH2OH*+*→CH2CHCH2*+OH* i361108+i000000-i350105+i011101	–0.71	0.08	–0.63	0.17	0.87	0.70
CH3CHCH2OH*+*→CH3CHCH2*+OH* i371103+i000000-i360102+i011101	–0.59	0.86	–0.57	0.94	0.33	0.37

Table S21. Hydrogenation reactions shown on **Figure S7** from LSR benchmarked against explicit DFT-NEB; Reaction and activation energies, ΔE and E_a, in eV, for selected C–H and O-H bond formation reactions at U = 0.0 V *vs*. RHE. DFT values without solvation are indicated with the "$_{DFT}$" subscript. Bader charge differences upon reaction, $\Delta\Delta Q_{B,\Delta E}$, and from the initial to the transition state, $\Delta Q_{B,Ea}$. Positive values indicate an increase in electronic density, thus the given step is promoted under reductive potentials. Activation energies calculated using LSR with solvent, $E_{a,LSR}$. The difference between LSR and DFT values is shown as err(E_a). The labels to find the respective transition states in the ioChem-BD database are indicated[9,10].

Reaction (top) Label ioChem-BD (bottom)	ΔE_{DFT} eV	$E_{a,DFT}$ eV	ΔE eV	E_a eV	$\Delta\Delta Q_{B,\Delta E}$ e$^-$	$\Delta\Delta Q_{B,Ea}$ e$^-$	$E_{a,LSR}$ eV	err(E_a) eV
$COCHCH_2$*+H*→$CHOCHCH_2$*+* i331102-i010101+i341104+i000000	-1.19	0.11	-1.19	0.17	0.15	0.22	0.37	0.20
$CHOCHCH_2$*+H*→$CHOCHCH_3$*+* i341104-i010101+i351102+i000000	-0.60	0.61	-0.55	0.67	-0.36	-0.10	0.60	-0.07
$CHOCHCH_3$*+H*→$CHOCH_2CH_3$*+* i351102-i010101+i361101+i000000	0.20	0.95	0.13	0.97	-0.81	-0.33	0.86	-0.11
$CHOCH_2CH_3$*+H*→$CH_2OCH_2CH_3$*+* i361101-i010101+i371101+i000000	-0.77	0.46	-0.67	0.53	0.24	0.10	0.56	-0.03
$CHOCHCH_2$*+H*→$CHOHCHCH_2$*+* i341104-i010101+i35110a+i000000	0.11	0.49	0.07	0.50	-0.68	-0.11	0.93	0.01
CHOCHCH3*+H*→$CHOHCHCH_3$*+* i351102-i010101+i361105+i000000	0.32	1.10	0.22	1.06	-0.92	-0.43	1.02	-0.04
$CHOCH_2CH_3$*+H*→$CHOHCH_2CH_3$*+* i361101-i010101+i371102+i000000	0.20	1.07	0.22	1.11	-0.19	-0.63	1.02	-0.08
$CH_2OCH_2CH_3$*+H*→$CH_2OHCH_2CH_3$*+* i371101-i010101+i381101+i000000	-0.06	0.89	-0.16	0.93	-0.85	-0.47	0.79	-0.14

Table S22. Reaction energies, ΔE, for decomposition of formaldehyde. DFT values without solvation are indicated with the "$_{DFT}$" subscript. Bader charge differences upon reaction, $\Delta\Delta Q_{B,\Delta E}$, are shown in e$^-$. Positive values indicate an increment in electronic density, thus promoting the given step under reductive potentials. The labels to find the respective transition states in the ioChem-BD database are indicated. Formaldehyde, thus, can hardly decompose into the more reactive moieties CH_2 or CHO, and their production of propylene (**Table 1**) can only be rationalised by aldol condensation[34].

Reaction (top) Label ioChem-BD (bottom)	ΔE_{DFT} / eV	ΔE / eV	$\Delta\Delta Q_{B,\Delta E}$ / e$^-$
CH_2O*+*→CH_2*+O*	0.36	0.33	0.99
CH_2O*+*→CHO*+H*	0.47	0.46	0.12

Table S23. Faradaic efficiencies (*FE*) and standard deviations (*Stdev.*) of products detected from the electrolysis of 50 mM propionaldehyde (C_3 reagent) on OD-Cu in 0.1 M potassium phosphate buffer (pH 7) at −0.4 V and −1.0 V *vs*. RHE for 60 min. The values shown are an average taken from three experiments.

Products	Propionaldehyde at –0.4 V		Propionaldehyde at –1.0 V	
	FE / %	*Stdev.* / %.	*FE* / %	*Stdev*. / %
Hydrogen	52.49	0.28	66.14	0.58
Propylene	0.08	0.02	0.09	0.0001
Propane	0.03	0.01	0.50	0.04
1-Propanol	39.92	0.03	10.89	3.06

Table S24. Faradaic efficiencies (*FE*) and standard deviations (*Stdev.*) of products detected from the electrolysis of 50 mM allyl alcohol (C_3 reagent) on OD-Cu in 0.1 M potassium phosphate buffer (pH 7) at −0.4 V and −1.0 V *vs*. RHE for 60 min. The values shown are an average taken from three experiments.

Products	Allyl alcohol at –0.4 V		Allyl alcohol at –1.0 V	
	FE / %	*Stdev.* / %.	*FE* / %	*Stdev*. / %
Hydrogen	75.73	6.60	78.78	3.28
Propylene	3.59	0.53	9.55	2.97
Propane	0.15	0.07	0.22	0.04
1-Propanol	13.71	2.43	2.00	0.61

References

1 G. Kresse and J. Hafner, *Phys. Rev. B*, 1993, **47**, 558–561.
2 J. P. Perdew, K. Burke and M. Ernzerhof, *Phys. Rev. Lett.*, 1996, **77**, 3865–3868.
3 S. Grimme, *J. Comput. Chem.*, 2006, **27**, 1787–1799.
4 N. Almora-Barrios, G. Carchini, P. Błoński and N. López, *J. Chem. Theory Comput.*, 2014, **10**, 5002–5009.
5 G. Kresse and D. Joubert, *Phys. Rev. B*, 1999, **59**, 1758–1775.
6 W. Luo, X. Nie, M. J. Janik and A. Asthagiri, *ACS Catal.*, 2016, **6**, 219–229.
7 Y. G. Kim, J. H. Baricuatro, A. Javier, J. M. Gregoire and M. P. Soriaga, *Langmuir*, 2014, **30**, 15053–15056.
8 G. Henkelman and H. Jónsson, *J. Chem. Phys.*, 2000, **113**, 9978–9985.
9 M. Álvarez-Moreno, C. De Graaf, N. López, F. Maseras, J. M. Poblet and C. Bo, *J. Chem. Inf. Model.*, 2015, **55**, 95–103.
10 R. García-Muelas, S. Pablo-García and N. López, *Dataset associated to: Mechanistic Routes toward C_3 products in Copper-Catalyzed CO_2 Electroreduction; DOI 10.19061/iochem-bd-1-175*, 2020.
11 M. Garcia-Ratés and N. López, *J. Chem. Theory Comput.*, 2016, **12**, 1331–1341.
12 M. Garcia-Ratés, R. García-Muelas and N. López, *J. Phys. Chem. C*, 2017, **121**, 13803–13809.
13 J. K. Nørskov, J. Rossmeisl, A. Logadottir, L. Lindqvist, J. R. Kitchin, T. Bligaard and H. Jónsson, *J. Phys. Chem. B*, 2004, **108**, 17886–17892.
14 A. A. Peterson, F. Abild-Pedersen, F. Studt, J. Rossmeisl and J. K. Nørskov, *Energy Environ. Sci.*, 2010, **3**, 1311–1315.
15 Q. Li, R. García-Muelas and N. López, *Nat. Commun.*, 2018, **9**, 526.
16 T. Cai, H. Sun, J. Qiao, L. Zhu, F. Zhang, J. Zhang, Z. Tang, X. Wei, J. Yang, Q. Yuan, W. Wang, X. Yang, H. Chu, Q. Wang, C. You, H. Ma, Y. Sun, Y. Li, C. Li, H. Jiang, Q. Wang and Y. Ma, *Science* 2021, **373**, 1523–1527.
17 R. B. Sandberg, J. H. Montoya, K. Chan and J. K. Nørskov, *Surf. Sci.*, 2016, **654**, 56–62.
18 M. Yu and D. R. Trinkle, *J. Chem. Phys.*, 2011, **134**, 64111.
19 R. García-Muelas, F. Dattila, T. Shinagawa, A. J. Martín, J. Pérez-Ramírez and N. López, *J. Phys. Chem. Lett.*, 2018, **9**, 7153–7159.
20 N. Yang, A. J. Medford, X. Liu, F. Studt, T. Bligaard, S. F. Bent and J. K. Nørskov, *J. Am. Chem. Soc.*, 2016, **138**, 3705–3714.
21 A. J. Medford, J. Wellendorff, A. Vojvodic, F. Studt, F. Abild-Pedersen, K. W. Jacobsen, T. Bligaard and J. K. Norskov, *Science (80-.).*, 2014, **345**, 197–200.
22 E. Walker, S. C. Ammal, G. A. Terejanu and A. Heyden, *J. Phys. Chem. C*, 2016, **120**, 10328–10339.
23 J. E. Sutton and D. G. Vlachos, *J. Catal.*, 2016, **338**, 273–283.
24 Douglas B. West, *Introduction to Graph Theory*, Pentice Hall, 2nd edn., 2001.
25 R. Garcia-Muelas, Q. Li and N. López, *ACS Catal.*, 2015, **5**, 1027–1036.
26 M. García-Mota, B. Bridier, J. Pérez-Ramírez and N. López, *J. Catal.*, 2010, **273**, 92–102.
27 H. Jónsson, G. Mills and K. W. Jacobsen, in *Classical and Quantum Dynamics in Condensed Phase Simulations*, WORLD SCIENTIFIC, 1998, pp. 385–404.
28 G. Henkelman, B. P. Uberuaga and H. Jónsson, *J. Chem. Phys.*, 2000, **113**, 9901–9904.
29 S. Pablo-García, M. Álvarez-Moreno and N. López, *Int. J. Quantum Chem.*, 2021, **121**, e26382.
30 J. Neugebauer and M. Scheffler, *Phys. Rev. B*, 1992, **46**, 16067–16080.
31 N. D. Lang and W. Kohn, *Phys. Rev. B*, 1973, **7**, 3541–3550.
32 D. Ren, J. Fong and B. S. Yeo, *Nat. Commun. 2018 91*, 2018, **9**, 925.
33 S. Nitopi, E. Bertheussen, S. B. Scott, X. Liu, A. K. Engstfeld, S. Horch, B. Seger, I. E. L. Stephens, K. Chan, C. Hahn, J. K. Nørskov, T. F. Jaramillo and I. Chorkendorff, *Chem. Rev.*, 2019, **119**, 7610–7672.

34 L. R. L. Ting, R. García-Muelas, A. J. Martín, F. L. P. Veenstra, S. T.-J. Chen, Y. Peng, E. Y. X. Per, S. Pablo-García, N. López, J. Pérez-Ramírez and B. S. Yeo, *Angew. Chemie Int. Ed.*, 2020, **59**, 21072–21079.
35 R. García-Muelas and N. López, *J. Phys. Chem. C*, 2014, **118**, 17531–17537.
36 Y. Hori, I. Takahashi, O. Koga and N. Hoshi, *J. Phys. Chem. B*, 2002, **106**, 15–17.
37 F. Dattila, R. García-Muelas and N. López, *ACS Energy Lett.*, 2020, **5**, 3176–3184.
38 F. Dattila, R. García-Muelas and N. López, *Dataset associated to: Active and Selective Ensembles in Oxide- Derived Copper Catalysts for CO_2 Reduction; DOI 10.19061/iochem-bd-1-165*, 2020.
39 P. J. Mallard and W. G. Linstrom, *'Thermodynamics source database'. NIST Chemistry WebBook, NIST Standard Reference Database Number 69. National Institute of Standards and Technology*, 2018.